









# Improving blazar redshift constraints with the edge of the Ly $\alpha$ forest: 1ES 1553+113 and implications for observations of the WHIM

J. Dorigo Jones <sup>1,2</sup>★, S. D. Johnson <sup>1</sup>★, Sowgat Muzahid <sup>3,4</sup>, J. Charlton <sup>5</sup>, H.-W. Chen <sup>6</sup>,  
A. Narayanan,<sup>7</sup> Sameer <sup>5</sup>, J. Schaye <sup>8</sup> and N. A. Wijers <sup>8</sup>

<sup>1</sup>Department of Astronomy, University of Michigan, 1085 South University Ave., Ann Arbor, MI 48109-1107, USA

<sup>2</sup>Department of Astrophysical and Planetary Sciences, University of Colorado Boulder, 391 UCB, 2000 Colorado Ave., Boulder, CO 80309, USA

<sup>3</sup>IUCAA, Post Bag-04, Ganeshkhind, Pune 411007, India

<sup>4</sup>Leibniz-Institut für Astrophysik Potsdam (AIP), An der Sternwarte 16, D-14482 Potsdam, Germany

<sup>5</sup>Department of Astronomy & Astrophysics, The Pennsylvania State University, 525 Davey Lab, University Park, PA 16802, USA

<sup>6</sup>Department of Astronomy & Astrophysics, The University of Chicago, 5640 South Ellis Avenue, Chicago, IL 60637, USA

<sup>7</sup>Indian Institute of Space Science and Technology, Thiruvananthapuram 695547, Kerala, India

<sup>8</sup>Leiden Observatory, Leiden University, PO Box 9513, NL-2300 RA Leiden, The Netherlands

Accepted 2021 November 11. Received 2021 November 1; in original form 2021 August 27

## ABSTRACT

Blazars are some of the brightest ultraviolet (UV) and X-ray sources in the sky and are valuable probes of the elusive warm-hot intergalactic medium (WHIM;  $T \simeq 10^5$ – $10^7$  K). However, many of the brightest blazars – called BL Lac objects such as 1ES 1553+113 – have quasi-featureless spectra and poorly constrained redshifts. Here, we significantly improve the precision of indirect redshift constraints for blazars based on the edge of the H I Ly  $\alpha$  forest observed in their UV spectra. We develop a robust technique to constrain the redshift of a  $z < 0.5$  active galactic nucleus (AGN) or blazar with a  $1\sigma$  uncertainty of  $\approx 0.01$  using only the position of its highest redshift Ly  $\alpha$  absorber with  $\log N_{\text{H}}/\text{cm}^{-2} > 12.6$ . We use a large sample of 192 AGNs/quasi-stellar objects at  $0.01 \lesssim z \lesssim 0.45$  that have high-quality Cosmic Origins Spectrograph (COS) far-UV spectra to characterize the intrinsic scatter in the gap between the AGN redshift and the edge of their Ly  $\alpha$  forest. We present new COS near-UV data for 1ES 1553+113 and confirm its redshift of  $z = 0.433$  using our technique. We apply our Ly  $\alpha$ -forest-based redshift estimation technique to nine additional blazars with archival *Hubble Space Telescope* UV spectra, most of which are key targets for future X-ray missions. Our inferred redshift constraints improve estimates for two BL Lacs (1ES 1118+424 and S5 0716+714) and are consistent with previous estimates for the rest. Our results emphasize the need to obtain further UV spectra of bright blazars, of which many have uncertain redshifts, in order to maximize the scientific value of future X-ray WHIM observations that will improve our understanding of galaxy evolution.

**Key words:** BL Lacertae objects: general – BL Lacertae objects: individual: 1ES 1553+113 – intergalactic medium – quasars: absorption lines.

## 1 INTRODUCTION

A number of active galactic nuclei (AGNs) have a relativistic jet that is oriented directly towards Earth, and the resulting beaming causes them to be some of the brightest objects observed in the Universe. These extreme AGNs, known as blazars, have been the catalyst for many discoveries in high-energy astrophysics and observational cosmology. Blazars can be extraordinarily bright in the ultraviolet (UV), X-ray, and even  $\gamma$ -ray, making them ideal background sources for absorption studies of the diffuse intergalactic medium (IGM; see reviews by Bregman 2007; McQuinn 2016) and also for constraints on the extragalactic background light (EBL) (see e.g. Stecker, Baring & Summerlin 2007; Biteau & Williams 2015 and the review by Madejski & Sikora 2016).

Blazars are particularly promising probes of the elusive warm-hot phase of the IGM (WHIM;  $T \simeq 10^5$ – $10^7$  K), which cosmological simulations predict contains up to  $\approx 50$  per cent of all baryons at low redshift ( $z \lesssim 1$ ; Cen & Ostriker 1999, 2006; Cui et al. 2019; Martizzi et al. 2019; Tuominen et al. 2021), with the other half of baryons residing in galaxies (Fukugita & Peebles 2004), the circumgalactic medium (CGM; see review by Tumlinson, Peebles & Werk 2017), the intracluster or intragroup medium (ICM or IGrM; Simionescu et al. 2011; Urban et al. 2011; Eckert et al. 2015), and the cooler photoionized IGM ( $T \simeq 10^4$ – $10^5$  K; Penton, Stocke & Shull 2004; Shull, Smith & Danforth 2012).

Detecting the WHIM beyond the Local Group (e.g. Bregman & Lloyd-Davies 2007; Anderson & Bregman 2010; Gupta et al. 2012; Miller & Bregman 2013; Fang et al. 2015; Qu et al. 2021) has been a significant observational challenge because of its low average density ( $n_{\text{H}} \lesssim 10^{-4} \text{ cm}^{-3}$ ) and high temperatures, leading to what is known as the ‘missing baryons’ problem at low redshift. Recently, the localization of fast radio bursts (FRBs) to their host galaxies has

\* E-mail: [johnny.dorigojones@colorado.edu](mailto:johnny.dorigojones@colorado.edu) (JJ); [seanjoh@umich.edu](mailto:seanjoh@umich.edu) (SJ)

enabled the likely closure of the missing baryon problem through the excess dispersion measure attributed to free electrons in the IGM (Bannister et al. 2019; Ravi et al. 2019; Macquart et al. 2020; Ocker, Cordes & Chatterjee 2021); however, there are only a few such localized FRBs (Walker, Ma & Breton 2020), and the dispersion contribution from the WHIM relative to the cool IGM is difficult to constrain directly (e.g. Shull & Danforth 2018; Medlock & Cen 2021) even when local and FRB host contributions are controlled for. This leaves important questions regarding the prevalence, distribution, phase, and metallicity of the WHIM largely unanswered. A more complete characterization of the WHIM is necessary not only as a check of our understanding of cosmic structure formation, but also to gain insight into galactic feedback and the flow of baryons through the CGM and IGM (e.g. Somerville & Davé 2015; Anglés-Alcázar et al. 2017; Peeples et al. 2019; Wijers et al. 2019; Wijers, Schaye & Oppenheimer 2020; Mitchell & Schaye 2021).

So far, only the lower temperature regime ( $T \simeq 10^5 - 10^{5.5}$  K) of the WHIM has been observed in large spectroscopic samples: through broad neutral hydrogen Lyman  $\alpha$  (H I Ly  $\alpha$ ) and O VI absorption in the far-UV (FUV) (Thom & Chen 2008; Tripp et al. 2008; Danforth et al. 2010; Narayanan et al. 2010; Shull et al. 2012; Tilton et al. 2012; Danforth et al. 2016). In smaller samples, Ne VIII absorption has been used to detect warm-hot baryon reservoirs primarily at  $z \gtrsim 0.5$  because of the available UV coverage (Meiring et al. 2013; Pachat et al. 2017; Frank et al. 2018; Burchett et al. 2019). At somewhat higher temperatures ( $T \gtrsim \text{few} \times 10^6$  K), the WHIM has been probed using the thermal Sunyaev–Zel’dovich effect around massive galaxies and clusters (de Graaff et al. 2019; Tanimura et al. 2019; Singari, Ghosh & Khatri 2020). These detections can account for about two-thirds of the expected baryon content of the WHIM, leaving  $\approx 18$  per cent of all baryons at low-redshift still elusive (de Graaff et al. 2019).

As such, the exhaustive search for and characterization of the hot phase of the WHIM currently relies on difficult-to-detect atomic transitions from highly ionized metals expected towards X-ray bright sightlines that probe  $T \gtrsim 10^6$  K gas. Some of the strongest expected tracers of the hot WHIM are intervening O VII  $\lambda 21.6$  Å and O VIII  $\lambda 18.9$  Å absorption lines in the X-ray (e.g. Hellsten, Gnedin & Miralda-Escudé 1998; Wijers et al. 2019). Possibilities exist in the FUV, such as the O VI  $\lambda \lambda 1031, 1037$  Å and Ne VIII  $\lambda \lambda 770, 780$  Å doublets (e.g. Mulchaey et al. 1996), but these ions are not unambiguous tracers of hot gas as they can be either photoionized or collisionally ionized (e.g. Thom & Chen 2008; Tripp et al. 2008; Savage et al. 2014; Hussain et al. 2017; Narayanan et al. 2018), and they would be harder to detect than O VII or O VIII at these temperatures given their decreasing ion fractions over the temperature range  $T \simeq 10^{5.5} - 10^6$  K (e.g. Oppenheimer & Schaye 2013).

Detections of the hot WHIM towards blazars in X-ray absorption have so far been contested, mainly as a result of the limited sensitivity and spectral resolution of available X-ray telescopes (Fang et al. 2002; Nicastro et al. 2005a,b; Kaastra et al. 2006; Bregman 2007; Fang et al. 2010; Ren, Fang & Buote 2014; Nicastro et al. 2016; Bregman et al. 2018). Recent X-ray follow-up studies of the UV-detected WHIM utilized stacking to obtain tentative detections of intervening O VII or O VIII absorption (Bonamente et al. 2016; Kovács et al. 2019; Nevalainen et al. 2019; Ahoranta et al. 2020), although the physical properties (e.g. metallicity, ionization state) of the absorbing gas are uncertain (see Bregman et al. 2019, and references therein). Indeed, direct detections of the hot WHIM in individual absorbers are currently limited to a few systems, but this will be revolutionized by future X-ray missions (see Wijers et al. 2020), such as *Athena* (approved, planned launch early 2030s, Barret et al. 2016), *Arcus*

(proposed, Smith et al. 2019), and *Lynx* (concept, Gaskin et al. 2018). This underscores the need to prepare sufficient sightlines of distant blazars that have well-determined redshifts and that are bright enough to probe the IGM via both UV and X-ray absorption spectroscopy (e.g. Bregman et al. 2015).

To probe the hot WHIM in absorption over the largest available redshift path-length, Nicastro et al. (2018) observed the bright, featureless blazar 1ES 1553+113 using 1.75 Ms of *XMM-Newton* grating spectroscopy. The exceptionally high signal-to-noise (S/N) X-ray spectrum of 1ES 1553+113 revealed two candidate O VII absorption systems along the line of sight at  $z = 0.4339$  and  $0.3551$  that were thought to arise from the WHIM. A census based on these candidate detections can account for the remaining ‘missing baryons’ (Nicastro 2018).

However, 1ES 1553+113 has no direct spectroscopic redshift measurement because its spectrum lacks any detected intrinsic absorption or emission lines. In order to place a limit on the redshift of 1ES 1553+113, Danforth et al. (2010) utilized the presence of intervening absorption in its FUV spectrum. They inferred a redshift constraint for 1ES 1553+113 of  $0.433 < z < 0.58$  by comparing the observed and expected H I Ly  $\alpha$  line densities. This was later corrected by Danforth et al. (2016) to be  $0.413 < z < 0.56$  after accounting for a previous line misidentification. Unfortunately, the large range in possible redshifts rendered the origin of the  $z = 0.4339$  candidate O VII absorber ambiguous.

In efforts to pin down the systemic redshift of 1ES 1553+113 and study absorber origins, Johnson et al. (2019) performed a deep spectroscopic redshift survey towards this blazar and inferred a statistical redshift constraint from its H I Ly  $\alpha$  forest and group environment. They found that 1ES 1553+113 is most likely a member of a galaxy group identified at  $z = 0.433$ . However, confirmation of this result requires further spectral coverage towards 1ES 1553+113 in the near-UV (NUV) and a more robust characterization of the edge of the observed Ly  $\alpha$  forest in order to unambiguously determine the redshift of this blazar.

In fact, many bright blazars, such as 1ES 1553+113, have no measured spectroscopic redshift. These quasi-featureless blazars, known as BL Lac objects, comprise approximately half of all known blazars, with the rest known as flat-spectrum radio quasars (FSRQs) (e.g. Healey et al. 2007; Falomo, Pian & Treves 2014; Mao & Urry 2017). Much work has been done to constrain the redshifts of BL Lac objects through both direct and indirect methods, such as detecting intrinsic but weak absorption or emission features from the blazar’s host galaxy or nucleus (e.g. Stocke, Danforth & Perlman 2011; Fang et al. 2014; van den Bosch et al. 2015; Archambault et al. 2016; Danforth et al. 2016; Paiano et al. 2017; Bu et al. 2019; Furniss et al. 2019; Goldoni et al. 2021; Paiano et al. 2021), associating the blazar with a nearby galaxy group (e.g. Farina et al. 2016; Rovero et al. 2016; Torres-Zafra et al. 2018; Johnson et al. 2019), or inferring a redshift constraint from the blazar’s highest-redshift H I Ly  $\alpha$  absorption line seen in the UV (e.g. Blades et al. 1985; Danforth et al. 2010, 2013; Furniss et al. 2013a,b; Johnson et al. 2019). For blazars at high redshift ( $z \gtrsim 1.3$ ), there is an additional redshift constraint tool in the photometric dropout method (Rau et al. 2012; Kaur et al. 2017; Rajagopal et al. 2020).

Accurate redshift constraints for featureless blazars are essential for interpreting studies of the WHIM in order to classify detected absorption systems as arising from either the IGM or the blazar’s group environment, the latter of which cannot be used for cosmological measurements. Studies of the EBL conducted towards bright blazars like 1ES 1553+113 also rely on well-constrained redshifts. In addition, Ly  $\alpha$  forest based redshift constraints may be useful

for studying other aspects of blazars, such as the unique class of gravitationally lensed blazars (e.g. Ostriker & Vietri 1985; Stickel, Fried & Kuehr 1988; Falomo, Melnick & Tanzi 1992; Readhead et al. 2021) in order to avoid confusion with features from the lensing galaxy.

Our goal in this paper is two-fold:

(i) verify the systemic redshift of IES 1553+113 with new NUV spectroscopy to better understand the origin of the X-ray absorbers detected towards this blazar, and

(ii) improve the quantification and precision of indirect redshift measurements for blazars based on the edge of the H I Ly  $\alpha$  forest in their spectra.

This paper proceeds as follows: In Section 2, we present new NUV observations of the blazar IES 1553+113 and confirm the extent of its Ly  $\alpha$  forest. In Section 3, we constrain the redshift of IES 1553+113 using its highest redshift Ly  $\alpha$  line in combination with a more complete characterization of the edge of the H I Ly  $\alpha$  forest observed in archival UV spectra of AGN at  $z \lesssim 0.45$ . We use this archival sample to evaluate statistical and systematic uncertainty in the redshift technique and compare to previous methods. In Section 4, we apply our redshift constraint technique to other well-known blazars and demonstrate its utility for future studies of the WHIM and for constraints on the EBL. We briefly summarize our conclusions in Section 5.

## 2 NUV OBSERVATIONS AND SPECTRAL ANALYSIS OF IES 1553+113

As summarized in the introduction, the redshift of IES 1553+113 must be constrained through indirect methods, because its intrinsic spectral features are currently undetectable. The highest redshift H I Ly  $\alpha$  absorption line seen towards IES 1553+113 in the FUV at  $z = 0.413$  has been used as a redshift lower limit to infer the blazar's membership with a galaxy group at  $z = 0.433$ , thus preventing the use of the  $z = 0.4339$  O VII candidate absorber in censuses of the WHIM (Johnson et al. 2019). However, given the position of the highest redshift Ly  $\alpha$  line detected relative to the end of the FUV spectrum (see Fig. 1), it is possible that a higher redshift Ly  $\alpha$  line could exist at  $z \gtrsim 0.46$ , seen in the NUV, which would invalidate the inferred redshift constraint.

Because of this, following Johnson et al. (2019), we obtained high-quality NUV spectra of IES 1553+113 with the Cosmic Origins Spectrograph (COS; Green et al. 2012) on the *Hubble Space Telescope* (HST) to search for H I Ly  $\alpha$  absorption at  $0.45 \lesssim z \lesssim 0.71$  (PI: Muzahid, PID: 15835, Muzahid et al. 2019). The absence of any such Ly  $\alpha$  absorption in the NUV would help to verify the galaxy group association inferred for IES 1553+113, while detection of additional Ly  $\alpha$  absorption in the NUV would imply that the blazar is located at higher redshift.

We acquired the NUV spectroscopy of IES 1553+113 over four orbits with the COS G185M grating using four central wavelength (CENWAVE) settings: 1882, 1913, 1941, and 1953 Å, each observed for one orbit, for a total of 8.7 ks of COS NUV spectroscopy. We split the observations in each CENWAVE setting into four exposures with different grating offset positions (FP-POS = 1–4) to minimize flat-fielding errors. The resulting 16 exposures provide contiguous spectral coverage from 1759 to 2079 Å, including some overlap with the COS FUV spectrum of IES 1553+113.

We performed the initial data reduction of these NUV observations using default parameters in the COS calibration pipeline (CALCOS, v3.3.9) to generate one-dimensional extracted spectra. The X1DCORR

module in CALCOS performs a BOXCAR spectral extraction on each NUV spectral stripe (i.e. NUVA, NUVB, NUVC) in the two-dimensional spectral image (i.e. flat-fielded image file) using values for the slope, y-intercept, and extraction box height (EBH) of each stripe for each CENWAVE setting (see Snyder & Sonnentrucker 2017)<sup>1</sup>. However, the default extraction values do not maximize the S/N in the one-dimensional spectra, primarily because the default EBH of 57 pixels was chosen to minimize flux loss instead.

To improve the S/N in the NUV spectrum of IES 1553+113, we modified the spectral extraction aperture used in the data reduction process. We fit the trace along each spectral exposure to update the y-intercept and slope values, and we ran a grid of EBH values ( $7 \leq \text{EBH} \leq 23$ ) to determine the optimal EBH. We decided to use EBH = 15 pixels for each stripe because this value maximizes the S/N by decreasing the noise from dark current without significant loss of signal. Finally, we removed pixels with data quality (DQ) flag > 4. These modifications improved the S/N per resolution element (resel) in the reduced spectra by 10–15 per cent compared to the default spectral extraction, resulting in a median S/N per resel of  $\approx 12$ .

We then continuum-normalized and median-combined the resulting 16 modified one-dimensional spectra to produce the final co-added NUV spectrum of IES 1553+113, displayed in Fig. 1. We note that the first orbit for the 1953 CENWAVE setting failed because of a guide star acquisition issue, and we subsequently obtained repeat observations at this CENWAVE setting three months later. Between these observations, IES 1553+113 decreased in NUV flux by  $\approx 25$  per cent, which is unsurprising given its known variability (e.g. Pandey et al. 2019; Dhiman et al. 2021). This dimming required us to continuum-normalize the individual stripe co-adds for each CENWAVE setting, using a low-order polynomial fit, before median-combining them to create the final co-added spectrum. We also confirmed that the CALCOS wavelength calibration (wavecal) is consistent with the expected accuracy of 15 km s<sup>-1</sup> for the NUV channel by measuring the centroids of low-ionization Milky Way (MW) transitions.

We observed no detectable H I Ly  $\alpha$  emission line in the archival FUV and new NUV spectra of IES 1553+113, and so we proceeded to search for H I Ly  $\alpha$  absorption that could be used as an indirect redshift constraint. We visually identified the absorption features present in the high-quality NUV spectrum of IES 1553+113 over the wavelength range  $1759 \text{ \AA} < \lambda < 2079 \text{ \AA}$ , corresponding to  $0.45 \lesssim z_{\text{Ly}\alpha} \lesssim 0.71$ . The spectrum contains absorption at  $z \approx 0$  from four low-ionization MW metal ions (Si II, Al III, Zn II, and Cr II), and also a C IV  $\lambda\lambda 1548, 1550 \text{ \AA}$  doublet arising from an absorbing system at  $z \approx 0.187$  (see Fig. 1). This intervening absorber is also detected in O VI, N V, C III, and H I in the FUV (Danforth et al. 2010), and ionization analysis of this system will be presented in a future work.

To verify these detections, characterize the sensitivity of the data, and identify any possible additional absorption features, we performed a blind search for absorption lines by quantifying our ability to detect absorption throughout our NUV spectrum. Our line-finding procedure steps through the spectrum on a fine grid in wavelength ( $\Delta z = 0.0001$ , corresponding to typical H I Ly  $\alpha$  absorber line widths of  $\approx 20$  km s<sup>-1</sup> at  $z \approx 0.4$  (e.g. Danforth et al. 2016)) and calculates the best-fitting Voigt profile and the corresponding line strength, line width, and associated uncertainties using a Markov chain Monte Carlo (MCMC) method. Specifically, at each step we fit

<sup>1</sup>Also see the recently released ‘COS Walkthrough Notebooks’ by Space Telescope Science Institute (STScI): <https://github.com/spacetelescope/notebooks/tree/master/notebooks/COS>

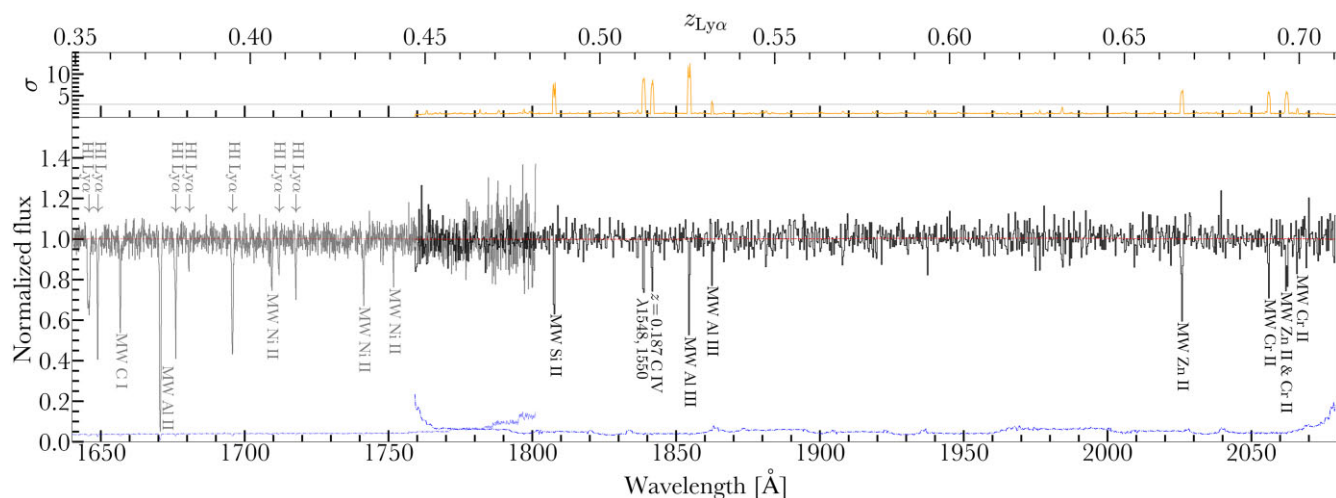


**Figure 1.** Co-added *HST/COS* NUV G185M spectrum of the blazar IES 1553+113 binned by 8 pixels, with normalized flux shown in black, error in blue, and the continuum in red. The bottom axis shows the observed-frame wavelength and the top axis shows the corresponding Ly  $\alpha$  redshift. Intervening H I Ly  $\alpha$  absorption systems and MW features are labelled, and the estimated significance of absorption line detection throughout the NUV spectrum is shown in the top panel in orange with the  $3\sigma$  significance level indicated by the horizontal grey line (see Section 2). The redward part of the COS FUV G160M spectrum of IES 1553+113 is shown in grey (Danforth et al. 2010; Johnson et al. 2019), which contains the highest redshift H I Ly  $\alpha$  line seen towards this blazar (see Section 2).

a Voigt profile with initial guesses for the line strength (i.e. column density multiplied by the transition cross-section:  $N \times \frac{\pi e^2}{m_e c} f_{jk}$ , where  $f_{jk}$  is the oscillator strength) and Doppler width ( $b$ ) that correspond to a typical H I Ly  $\alpha$  line (initial guesses:  $\log N_{\text{H I}}/\text{cm}^{-2} = 13.5$  and  $b = 15 \text{ km s}^{-1}$ ). The best-fitting values for line strength,  $b$ , and the centroid are calculated at each step by maximizing the likelihood function. The likelihood function is combined with our priors ( $10 \text{ km s}^{-1} < b < 50 \text{ km s}^{-1}$ ,  $\log N_{\text{H I}}/\text{cm}^{-2} > 11$ ) to create the full log likelihood function, which is then sampled at each wavelength step via MCMC using the EMCEE module (Foreman-Mackey et al. 2013) for a total of 3000 steps with a burn-in period of 2000 steps. We then computed the statistical significance,  $\sigma$ , of any absorption line detection as a function of wavelength in our NUV spectrum, shown in the top panel in Fig. 1.

This blind search recovers our manual line identifications at  $\sigma \gtrsim 3$  and does not return any additional lines. The  $3\sigma$  detection limit corresponds to a minimum detected H I column density in our NUV spectrum of  $\log N_{\text{H I}}/\text{cm}^{-2} \gtrsim 12.6$ . The only manual line identification not recovered at  $\sigma \gtrsim 3$  is the weaker MW Cr II line, but we note that this is indeed a commonly observed line in high H I column density systems (e.g. Mas-Ribas et al. 2017).

Most notably, we find no new H I Ly  $\alpha$  absorption in the NUV. This confirms the lower limit constraint on the blazar’s redshift of  $z_{\text{sys}} \gtrsim 0.413$  based on the position of its highest redshift H I Ly  $\alpha$  line in the FUV, seen in Fig. 1 (Danforth et al. 2016; Johnson et al. 2019). In order to infer a redshift upper limit constraint for IES 1553+113, or any blazar, based on its highest redshift Ly  $\alpha$  line, in the following section we closely examine the edge of the Ly  $\alpha$  forest observed towards low-redshift AGN with systemic redshifts available in the literature.

### 3 REDSHIFT CONSTRAINT BASED ON THE EDGE OF THE OBSERVED H I LY $\alpha$ FOREST

In this section, we develop and explore systematics of AGNs and blazar redshift constraints based on the highest redshift H I Ly  $\alpha$  absorption line observed in their spectra. In Section 3.2, we apply this redshift constraint technique to IES 1553+113 and confirm its

inferred galaxy group association. In Sections 3.3 and 3.4, we discuss the systematics of our technique, and in Section 3.5 we compare it to previous methods.

#### 3.1 AGN redshift constraints from the Ly $\alpha$ forest at $z \lesssim 0.45$

To develop our redshift constraint technique, we carry out a robust characterization of the edge of the H I Ly  $\alpha$  forest in a large sample of 192 AGNs at  $0.01 \lesssim z \lesssim 0.45$  with FUV spectra available in the COS archive. The redshift upper limit of  $z \lesssim 0.45$  is chosen to ensure COS coverage of the entire Ly  $\alpha$  forest towards the AGN. Each of these AGNs has a spectroscopic redshift measured from intrinsic emission lines, which enables us to construct an empirical cumulative distribution function of the difference between the AGN systemic redshifts and that of the highest redshift Ly  $\alpha$  absorption line in their UV spectra.

We construct our sample of Ly  $\alpha$  forest sightlines by retrieving the public data for all of the 584 AGNs/quasi-stellar objects (QSOs) in the Hubble Spectroscopic Legacy Archive (HSLA; Peeples et al. 2017) that have COS FUV coverage in the G130M or G160M gratings (as of 2020 October). We discarded all objects that have median S/N per resel  $< 10$  within  $5 \text{ \AA}$  of the Ly  $\alpha$  emission line to ensure a detection limit comparable to or better than our NUV spectrum of IES 1553+113 (see Section 2 and below), leaving 205 AGNs. We dropped nine of these AGNs because they were targeted to study broad associated absorption lines (BALs or mini-BALs) from outflows, which could skew the sample away from typical AGN. One object was dropped due to significant contamination from the MW Ly  $\alpha$  damping wing. We also dropped three objects that are blazars because we later apply the resulting redshift constraint to these objects (see Section 4.1). The final sample consists of 192 AGNs/QSOs (see Table 1), located at  $z \lesssim 0.45$ , which we use to characterize the edge of the observed H I Ly  $\alpha$  forest relative to the systemic redshift of the AGN.

We retrieved systemic redshifts,  $z_{\text{sys}}$ , for the sample from the literature by first finding matches in the Sloan Digital Sky Survey (SDSS) Quasar Catalogue (Schneider et al. 2007; P aris et al. 2017; Lyke et al. 2020), then in the UV-Bright Quasar Survey (UVQS)

**Table 1.** Low-redshift AGN/QSOs with high-quality *HST*/COS FUV data used for the redshift constraint technique.

Name <sup>a</sup>	$z_{\text{sys}}$ <sup>b</sup>	$\max(z_{\text{Ly}\alpha})$ <sup>c</sup>	$z_{\text{source}}^d$	<i>HST</i> proposal ID	Measurement flag <sup>e</sup>
HE 0153–4520	0.451	0.4284	VCV	11541	1
PG 0003+158	0.4509	0.4466	Hintzen (1984)	12038	1
SDSS J080359.23+433258.4	0.4489	0.4481	SDSS	11598	1
TON 236	0.4473	0.4480	SDSS	12038	1
SDSS J161649.42+415416.3	0.4412	0.4352	SDSS	11598	0
...	...	...	...	...	...

Notes. Table 1 is available online in its entirety in machine-readable format.

<sup>a</sup>Object ID, from HSLA (see Section 3.1).

<sup>b</sup>Systemic redshift of the AGN (see Section 3.1).

<sup>c</sup>Highest redshift Ly  $\alpha$  line with  $\log N_{\text{H I}}/\text{cm}^{-2} > 12.6$  detected in FUV spectrum of AGNs (see Section 3.1). For three of the objects that have  $\max(z_{\text{Ly}\alpha}) > z_{\text{sys}}$  (HB 89-202-765, SDSS J104741.75+151332.2, and SDSS J213357.89–071217.3), the  $\max(z_{\text{Ly}\alpha})$  measurement is somewhat uncertain and may be lower, but this does not change our results.

<sup>d</sup>Source of  $z_{\text{sys}}$  (see Section 3.1).

<sup>e</sup>‘1’ indicates a direct measurement of  $\max(z_{\text{Ly}\alpha})$ ; ‘0’ indicates the  $\max(z_{\text{Ly}\alpha})$  is a right-censored limit due to spectral quality issues (see Section 3.1).

DR1 (Monroe et al. 2016), then in the 13th edition of the Catalogue of Quasars and AGN by Véron-Cetty and Véron (VCV; Véron-Cetty & Véron 2010). For the 74 objects with no match in SDSS or UVQS, we used the most accurate spectroscopic redshift given in the NASA/IPAC Extragalactic Database (NED) if more accurate than the redshift from VCV. In the final sample, 95 objects use  $z_{\text{sys}}$  from SDSS, 27 from VCV, 23 from UVQS, 13 from the 6dF Galaxy Survey DR3 (Jones et al. 2009), and 34 from various other sources.<sup>2</sup> While the quality of the literature redshifts varies, they are all based on rest-frame optical emission lines, such as the Balmer series, [O II], [O III], and Mg II, which have typical systematic uncertainties of  $\approx 75$  km s<sup>-1</sup>, based on a comparison between Mg II and [O III] by Hewett & Wild (2010).

We identified the highest redshift Ly  $\alpha$  line,  $\max(z_{\text{Ly}\alpha})$ , in each AGN spectrum by fitting a single-component Voigt profile, making sure not to choose  $z \approx 0$  MW lines. In order to avoid misidentifying a  $z > 0$  metal line as H I Ly  $\alpha$ , we tested other possible line identifications and searched for the corresponding H I Ly  $\alpha$  line at the same redshift. This process confirms confident  $\max(z_{\text{Ly}\alpha})$  identifications, except in a few ambiguous cases, which do not affect our results (HB89-0202-765, SDSS J104741.75+151332.2, and SDSS J213357.89–071217.3, see Table 1). For AGN with  $\max(z_{\text{Ly}\alpha})$  at  $z \gtrsim 0.15$ , we confirmed the detection with the corresponding Ly  $\beta$  line. Also, for 54 AGNs ( $\approx 28$  per cent of the sample), we confirmed our  $\max(z_{\text{Ly}\alpha})$  by comparing with line identifications from Danforth et al. (2016).<sup>3</sup> We required the  $\max(z_{\text{Ly}\alpha})$  to have  $\log N_{\text{H I}}/\text{cm}^{-2} > 12.6$  and spectral S/N per resel  $> 10$  in order to obtain  $3\sigma$  detections.<sup>4</sup>

<sup>2</sup>Allen et al. (1978), Bergeron et al. (1983), Schmidt & Green (1983), Hintzen (1984), Remillard et al. (1986), Dressler & Shectman (1988), de Vaucouleurs et al. (1991), Fouqué et al. (1992), Huchra et al. (1993), Corwin Harold, Buta & de Vaucouleurs (1994), Marziani et al. (1996), Pietsch et al. (1998), Huchra, Vogeley & Geller (1999), Falco et al. (1999), Wisotzki et al. (2000), Springob et al. (2005), Ho & Kim (2009), Huchra et al. (2012).

<sup>3</sup><https://doi.org/10.17909/T95P4K>

<sup>4</sup>Even though our line selection criteria for  $\max(z_{\text{Ly}\alpha})$  reflect the  $3\sigma$  confidence limit for detecting absorption lines in our NUV spectrum of IES 1553+113, it is important to ensure that the chosen S/N cut and minimum  $\log N_{\text{H I}}$  are consistent such that we can confidently detect and measure unblended Ly  $\alpha$  stronger than the chosen limit in the AGN spectra. To test this, we calculated the median  $3\sigma$  limit for absorption line detection (see Section 2 for description of procedure) in the regions between  $\max(z_{\text{Ly}\alpha})$  and  $z_{\text{sys}}$  for the 16 AGNs with the lowest S/N spectra (i.e. S/N per resel  $< 20$ – $30$  near the Ly  $\alpha$  emission) and also for the 10 AGNs with  $\max(z_{\text{Ly}\alpha})$  most separated from the AGN (i.e.  $\Delta v = [c z_{\text{sys}} - c \max(z_{\text{Ly}\alpha})]/(1 + z_{\text{sys}})$

Finally, we computed the difference between the AGN systemic redshift and its highest redshift H I Ly  $\alpha$  absorption line for the entire sample:  $\Delta z = z_{\text{sys}} - \max(z_{\text{Ly}\alpha})$ . The observed cumulative distribution function (CDF) of this data set is shown in Fig. 2, which thus depicts the intrinsic scatter in the gap between low-redshift AGN/QSO systemic redshifts and their highest redshift H I Ly  $\alpha$  absorption line. Negative values in Fig. 2 are AGNs with an associated Ly  $\alpha$  line beyond their systemic redshift [i.e.  $\max(z_{\text{Ly}\alpha}) > z_{\text{sys}}$ ]; there are six AGNs in our sample with a  $\max(z_{\text{Ly}\alpha})$  offset by  $\Delta v < -1000$  km s<sup>-1</sup> (i.e.  $\Delta z \lesssim -0.004$ ), which could arise from unusually large redshift uncertainty, uncertain line identification, or from interesting, possibly inflowing, gas motions (see Table 1).

The 95 per cent confidence interval (CI) of this distribution can be used as a robust statistical constraint on the redshift,  $z$ , of any low-redshift AGN/QSO, when combined with the position of its UV-detected  $\max(z_{\text{Ly}\alpha})$  of  $\log N_{\text{H I}}/\text{cm}^{-2} > 12.6$ :

$$z_{95} = [\max(z_{\text{Ly}\alpha}) - 0.0047, \max(z_{\text{Ly}\alpha}) + 0.0224]. \quad (1)$$

The median of the distribution can also be used as an empirical redshift estimate, with two-sided error bars corresponding to the  $1\sigma$  error (i.e. 68 per cent CI):

$$z_{\text{med}} = \max(z_{\text{Ly}\alpha}) + 0.0006^{+0.0109}_{-0.0015}. \quad (2)$$

In creating the observed cumulative distribution of  $\Delta z = z_{\text{sys}} - \max(z_{\text{Ly}\alpha})$  shown in Fig. 2, we employed standard survival statistics to include 21 AGNs ( $\approx 11$  per cent of the sample) for which spectral quality issues enable only limits on  $\max(z_{\text{Ly}\alpha})$  by treating the point where the spectrum S/N falls below 10 or where contamination begins as a right-censored data point on  $\Delta z$  (see last column of Table 1). Of these 21 AGNs, six (6) have  $\max(z_{\text{Ly}\alpha})$  with spectral S/N per resel  $< 10$  (i.e. the spectrum falls below S/N  $\approx 10$  between  $\max(z_{\text{Ly}\alpha})$  and  $z_{\text{sys}}$ ), five (5) have a  $3\sigma$  detection limit slightly worse than our NUV spectrum of IES 1553+113,<sup>4</sup> and 10 AGN spectra contain contamination from geocoronal emission or poor/missing data between  $\max(z_{\text{Ly}\alpha})$  and  $z_{\text{sys}}$ . The distribution in Fig. 2 is thus a Kaplan–Meier curve, computed using LIFELINES (Davidson-Pilon

$> 3000$  km s<sup>-1</sup>). We found that only five of the low-S/N objects have a  $3\sigma$  detection limit slightly worse than our NUV spectrum of IES 1553+113 (i.e. minimum detected  $\log N_{\text{H I}}/\text{cm}^{-2} \gtrsim 12.6$ ). All of the other AGNs tested have a  $3\sigma$  detection limit better than our NUV spectrum, and the remaining, higher-S/N objects in our sample that were not tested would have even better detection limits. As such, these five AGNs are included as right-censored data points, as described in the text.

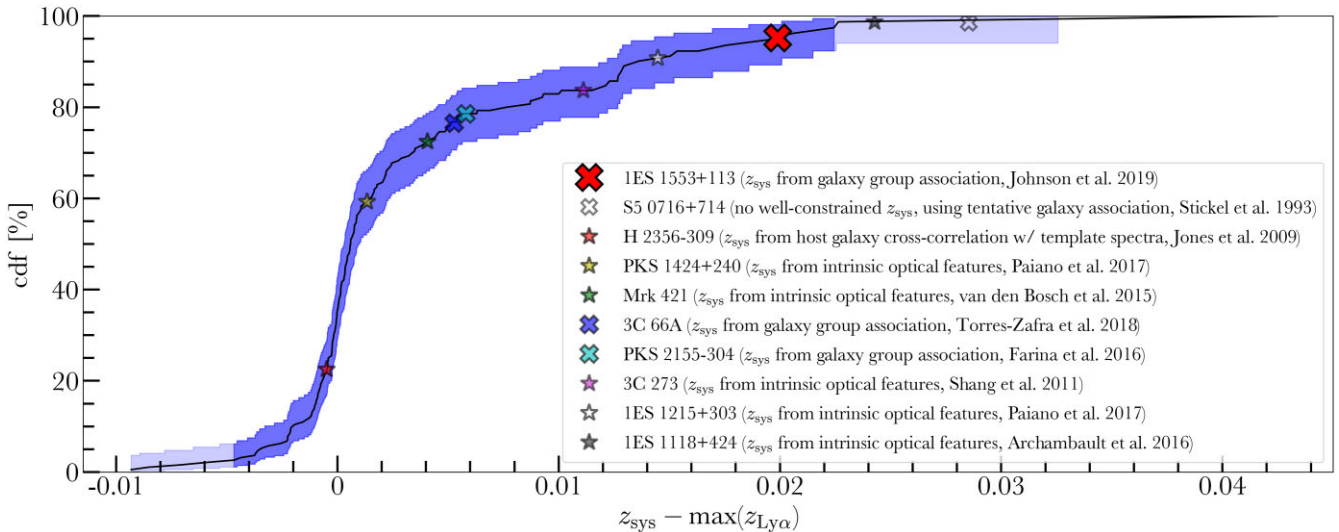


**Figure 2.** Observed cumulative distribution of the difference between the systemic redshift of an AGN and the highest redshift H I Ly  $\alpha$  absorption line observed towards it,  $\Delta z = z_{\text{sys}} - \max(z_{\text{Ly}\alpha})$ , for 192 AGNs located at  $0.01 \lesssim z \lesssim 0.45$  (see Section 3.1, Table 1). This distribution thus characterizes the intrinsic scatter in the gap between low-redshift AGNs/QSOs and the edge of their Ly  $\alpha$  forest. The 95 per cent confidence interval is highlighted in darker colour, which can be used as a robust redshift estimator when combined with an object’s UV-detected  $\max(z_{\text{Ly}\alpha})$  (see equation 1). The 10 blazars to which we apply our redshift constraint technique are shown by various symbols according to the legend (see Sections 3.2, 4, and Table 2).

et al. 2021), which is a non-parametric estimator of the CDF (see e.g. Isobe, Feigelson & Nelson 1986).

### 3.2 Redshift of IES 1553+113 and Implications for the WHIM

In Section 2, we verified the redshift lower limit of IES 1553+113 from its highest redshift Ly  $\alpha$  line; however, confirmation of its membership with a galaxy group at  $z = 0.433$  requires greater certainty in the inferred upper limit for the blazar’s redshift based on the edge of the Ly  $\alpha$  forest observed towards it (see Section 3.5).

We apply our redshift constraint technique obtained in Section 3.1 to IES 1553+113 using its confirmed highest redshift Ly  $\alpha$  line [i.e. equation (1) with  $\max(z_{\text{Ly}\alpha}) = 0.4131$ ] to infer a new 95 per cent confidence interval for its redshift of  $z = 0.408\text{--}0.436$ . The red X symbol in Fig. 2 at the  $\approx 95$ th percentile shows the position of IES 1553+113 within the inferred 95 per cent confidence interval.

Our empirical redshift constraint for IES 1553+113 improves the certainty in its inferred redshift upper limit (see Section 3.5) and confirms the blazar’s membership with a  $z = 0.433$  galaxy group identified in the deep spectroscopic redshift survey performed by Johnson et al. (2019). The stronger candidate O VII absorber detected towards IES 1553+113 at  $z = 0.4339$  (Nicastro et al. 2018) most likely arises from the CGM or IGrM of the blazar’s host environment and cannot be used for the census of warm-hot baryons in the sheets/filaments of the cosmic web (see absorber analysis in Johnson et al. 2019). Although the available sample of extragalactic X-ray absorption spectra is small, this suggests that the WHIM is not sufficiently metal enriched or is too low density to be detected in O VII or O VIII with current X-ray facilities (see e.g. Bregman et al. 2019; Nicastro et al. 2021), except possibly via spectral stacking (e.g. Kovács et al. 2019; Ahoranta et al. 2020, also see Ahoranta et al. 2021). In any case, further X-ray spectroscopy of AGNs and blazars with well constrained redshifts and complementary UV spectra and deep galaxy surveys are necessary in order to improve our understanding of the physical properties of the WHIM and its relationship to galaxy feedback and evolution.

### 3.3 Systematics of the redshift constraint technique

In this subsection, we discuss and quantify systematic uncertainties in our blazar redshift constraint technique that may arise from differences between blazars and typical AGN/QSOs due to local environment (Section 3.3.1) and the proximity effect (Section 3.3.2). We investigate systematic effects that could cause blazars to have an altered distribution of  $\Delta z = z_{\text{sys}} - \max(z_{\text{Ly}\alpha})$  compared to the one for AGNs/QSOs shown in Fig. 2. In particular, given that most of the AGN in our sample have a  $\max(z_{\text{Ly}\alpha})$  that would be considered associated or intrinsic (see Fig. 2), we focus on quantifying any potential difference in the incidence of associated absorption in the spectra of blazars (e.g. Ghisellini et al. 2011; Chand & Gopal-Krishna 2012; Mishra et al. 2019; Massaro et al. 2020) compared to AGN (e.g. Ganguly et al. 2013; Joshi, Chand & Gopal-Krishna 2013; Muzahid et al. 2013; Chen et al. 2018).

#### 3.3.1 The impact of local environment

We first consider the impact that known differences in the local environments of blazars and AGNs could have on their frequency of associated H I absorbers. To do this, we examined separately the distributions of  $\Delta z = z_{\text{sys}} - \max(z_{\text{Ly}\alpha})$  for radio-loud and radio-quiet AGNs, as radio-loud AGNs reside in more overdense environments (e.g. Retana-Montenegro & Röttgering 2017), similar to those typical of blazars (e.g. Allevalo, Finoguenov & Cappelluti 2014). Indeed, BL Lac objects reside in galaxies that are on average more massive than AGN/QSO host galaxies (see e.g. Urry et al. 2000 and the review by Falomo et al. 2014), which could possibly result in a different distribution of associated absorbers.

We cross-correlated our AGN sample with the Catalog of Quasar Properties from SDSS DR7 (Shen et al. 2011) to determine which objects have radio measurements from the FIRST survey (Helfand, White & Becker 2015). Adopting the definition for radio-loudness from Kellermann et al. (1989), we identified 16 radio-loud AGNs and 60 confirmed radio-quiet AGNs in our sample. We find that the radio-loud and radio-quiet AGNs have very similar distributions of  $\Delta z =$

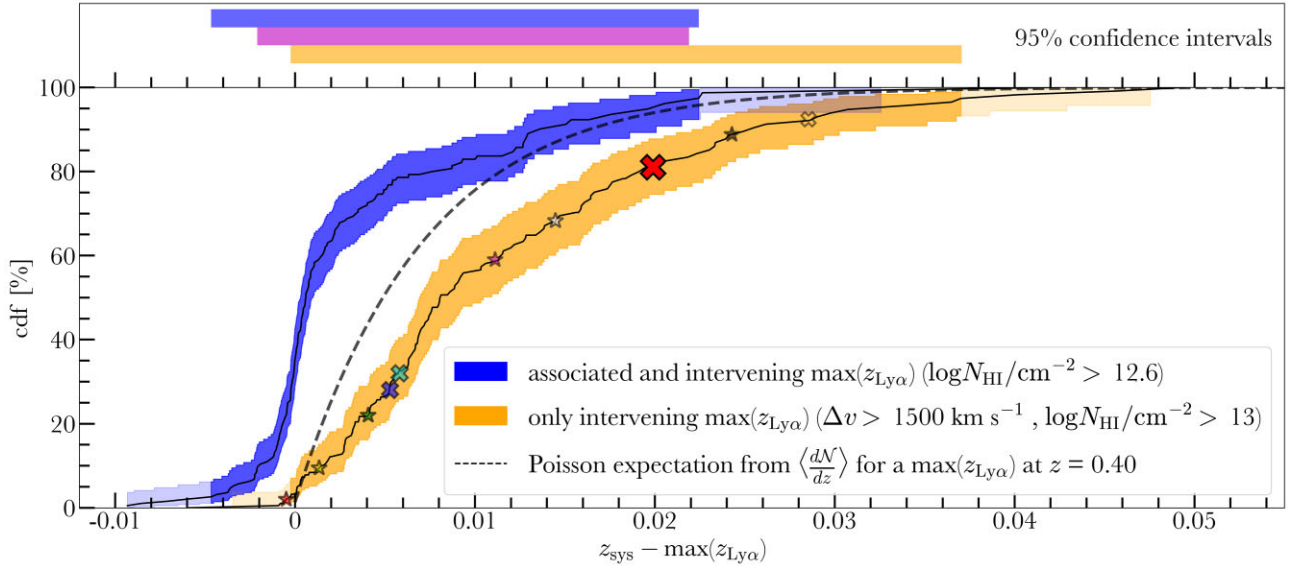


**Figure 3.** Cumulative distributions of  $\Delta z = z_{\text{sys}} - \max(z_{\text{Ly}\alpha})$  as described in Fig. 2. The blue distribution is the same as in Fig. 2, and the orange distribution represents a conservative estimate of the systematic uncertainty in the redshift constraint due to the proximity effect (see Section 3.3.2). The orange curve is obtained using only the highest redshift intervening Ly  $\alpha$  lines with  $\log N_{\text{HI}}/\text{cm}^{-2} > 13$  (see definition in the main text), shifted to  $\Delta z = 0$  to be used as an approximately unbiased redshift constraint in the case that blazars have a lower incidence of associated Ly  $\alpha$  (see Section 3.3). The 10 blazars to which we apply our redshift constraint technique are shown on the orange curve by various symbols according to the legend in Fig. 2 to represent their alternative redshift constraints than the ones adopted in Section 4 (see Section 3.3 and Table 2). The black dashed curve shows the expectation from Poisson statistics calculated based on the probability of observing no H I Ly  $\alpha$  lines as a function of  $\Delta z$  assuming the  $\frac{dN}{dz}$  measurement from Danforth et al. 2016 at  $z = 0.40$  (see Section 3.3.3). The top panel compares our empirical redshift constraints to the constraint from Johnson et al. (2019), which shares the same methodology: blue – ours (mostly associated and some intervening Ly  $\alpha$ , Section 3.1); orange – ours (only intervening Ly  $\alpha$ , see Section 3.3.2); purple – Johnson et al. (2019) (based on a reference AGN sample  $\approx 1/3$  the size of ours, mostly associated and some intervening Ly  $\alpha$ , see Section 3.5). We also note that our methodology results in a redshift constraint that is  $\approx 5\times$  tighter than previous methods used to constrain blazar redshifts from their H I Ly  $\alpha$  forest (Danforth et al. 2010, see Section 3.5).

$z_{\text{sys}} - \max(z_{\text{Ly}\alpha})$ . Performing a two-sample Kolmogorov–Smirnov (K–S) test yields a statistic of 0.167 with  $p$ -value of 0.82, although it is important to note that the sample size of radio AGN is likely too small to detect any significant difference between the  $\Delta z$  distributions. The median  $\Delta z$  of the radio-quiet AGNs is 0.001 compared to the median of 0.000 02 for the radio-loud AGNs. The difference between these median  $\Delta z$  values is  $\approx 5\times$  less than the scatter of the distributions. This confirms that the difference in local environment between blazars and AGNs does not have a significant effect on their observed distributions of  $\Delta z$ , and so does not contribute to systematics of the redshift constraint technique.

### 3.3.2 The impact of the proximity effect

While the presence of associated absorbers in AGN and blazar spectra is expected to tighten the  $\Delta z$  distribution, the proximity effect (e.g. Bajtlik, Duncan & Ostriker 1988; Kulkarni & Fall 1993; Bechtold 1994; Pascarelle et al. 2001; Calverley et al. 2011) due to enhanced ionization radiation near the AGN can decrease the incidence of absorbers that would broaden the distribution. Moreover, because blazars are more highly variable than typical AGN, the proximity effect around them may be different due to increased importance of non-equilibrium effects. To quantify the potential impact of the proximity effect on Ly  $\alpha$  absorption inferred redshifts, we first searched for a trend between AGN luminosity and  $\Delta z$  and then placed a conservative upper limit on the potential impact of the proximity effect by examining a spectral region where it is significant.

To determine whether the proximity effect can bias Ly  $\alpha$  inferred redshifts, we calculated the generalized Kendall rank correlation coefficient between the AGN UV luminosity (Bianchi 2014) and  $\Delta z = z_{\text{sys}} - \max(z_{\text{Ly}\alpha})$  and found  $\tau = +0.13$  with a marginal significance of 0.04. Moreover, this weak correlation is largely driven by the three lowest luminosity AGNs in the sample. This experiment demonstrates that the proximity effect does not contribute significantly to the systematic uncertainty in Ly  $\alpha$  inferred redshifts for non-blazar AGNs.

Blazars are significantly more variable than typical AGN, which may result in a difference in proximity effect caused by non-equilibrium effects. To ensure that our Ly  $\alpha$  inferred blazar redshifts are robust, we placed a conservative upper limit on systematic uncertainty resulting from the proximity effect by remeasuring the  $\Delta z$  distribution after excluding the spectral region that corresponds to H I Ly  $\alpha$  velocities within  $1500 \text{ km s}^{-1}$  of the AGN systemic. By identifying only  $\max(z_{\text{Ly}\alpha})$  that are at  $\Delta v > 1500 \text{ km s}^{-1}$  from each AGN, we maximize the spread in the  $\Delta z$  distribution because associated absorbers are less common in this velocity range while the proximity effect remains significant (e.g. Fox, Bergeron & Petitjean 2008; Tripp et al. 2008).

The S/N available in the archival COS AGN spectra are lower at  $|\Delta v| > 1500 \text{ km s}^{-1}$  from the AGN systemic velocity because of the weaker Ly  $\alpha$  emission away from the line peak. Consequently, when making the ‘intervening only’  $\Delta z$  distribution, we adopted a higher threshold in column density of  $\log N_{\text{HI}}/\text{cm}^{-2} > 13$  to ensure high completeness rates. Finally, we shifted the resulting  $\Delta z$  distribution by  $-0.006$  in redshift, which corresponds to  $\Delta v = -1500 \text{ km s}^{-1}$  at the median systemic redshift of our AGN sample. This ensures that

the resulting cumulative distribution can be used as an approximately unbiased estimator of AGN and blazar redshifts.

The resulting ‘intervening only’ distribution is shown in orange in Fig. 3. If this curve is adopted to infer redshifts, the resulting 95 per cent confidence interval and median would be:

$$z_{95} = [\max(z_{\text{Ly}\alpha}) - 0.0003, \max(z_{\text{Ly}\alpha}) + 0.0370] \quad (3)$$

and

$$z_{\text{med}} = \max(z_{\text{Ly}\alpha}) + 0.0080^{+0.0138}_{-0.0052}. \quad (4)$$

The resulting redshift constraints [i.e. equations (1) and (2), and (3) and (4)] differ in the median by less than the  $1\sigma$  uncertainty given in equation (2). Therefore, we have shown that the edge of the Ly  $\alpha$  forest can be used to set a robust statistical constraint on the redshift of AGNs and blazars with a statistical  $1\sigma$  uncertainty of  $\approx 0.01$  and with sub-dominant systematic uncertainty coming from any differences in the frequency of associated absorption and/or the proximity effect.

### 3.3.3 Analytical comparison

To provide an analytical comparison to the observed CDFs of  $\Delta z = z_{\text{sys}} - \max(z_{\text{Ly}\alpha})$  shown in Fig. 3, we use Poisson statistics to calculate the probability of observing no Ly  $\alpha$  absorption lines as a function of  $\Delta z$  when expecting to observe the mean number of intervening H I systems per unit redshift,  $\langle \frac{dN}{dz} \rangle$  (also see Blades et al. 1985; Furniss et al. 2013a). We adopt the redshift-dependent  $\frac{dN}{dz}$  measurement from Danforth et al. (2016), expressed as  $\frac{dN(>N,z)}{dz} = C_0(1+z)^\gamma$ , where  $C_0 = 91 \pm 1$  and  $\gamma = 1.24 \pm 0.04$  (see their fig. 13), and we use this to calculate the probability mass function as  $P(z) = \frac{\lambda^k e^{-\lambda}}{k!}$ , where  $k = 0$  and  $\lambda = \langle \frac{dN}{dz} \rangle \times [z - \max(z_{\text{Ly}\alpha})]$ . The resulting expected Poisson-based CDF is plotted in Fig. 3 for  $\max(z_{\text{Ly}\alpha}) = 0.4$ .

We see that the Poisson-based CDF is qualitatively similar to the two observed CDFs, falling in between them. The blue cumulative distribution appears to the left of the expected CDF because it is created using mostly associated  $\max(z_{\text{Ly}\alpha})$ , which drives it to lower, and even negative, values of  $\Delta z$ . The orange cumulative distribution appears more similar in shape to the expected CDF, but it is none the less driven to slightly larger values of  $\Delta z$ . Because the two distributions are obtained using the same minimum detected column density for intervening H I, the observed difference between them is likely due to the proximity effect near AGN (see Section 3.3.2).

### 3.4 The impact (and benefit) of IGM evolution

The number of Ly  $\alpha$  absorbers per unit redshift evolves both because of the expansion of the Universe and physical evolution of Ly  $\alpha$  forest clouds (e.g. Rauch 1998). Consequently, we expect both the median and scatter in the gap between AGN systemic redshifts and the highest redshift Ly  $\alpha$  absorber in their spectra to evolve with redshift. To estimate the significance of this evolution, we re-evaluated the CDFs for all (see Fig. 2) and intervening (see Fig. 3) absorbers after splitting the AGN sample by redshift at  $z = 0.2$ .

Somewhat surprisingly, when using both associated and intervening absorbers, the CDF does not change significantly. This suggests that the frequency of associated absorbers does not evolve over the relevant redshift range. For this reason, we adopt equations (1) and (2) as our preferred redshift estimators and use them even at a somewhat higher redshift in Section 4.1. On the other hand, the change in the CDF formed from intervening-only absorbers with  $\Delta v$

$> 1500 \text{ km s}^{-1}$  is more significant. In particular, for AGN with  $z < 0.2$ , we find  $dz_{\text{med}} = 0.009$  and an upward going  $1\sigma$  uncertainty of  $+0.022$ . For AGNs at  $z = 0.2-0.45$ , these decrease to  $dz_{\text{med}} = 0.007$  and a  $1\sigma$  uncertainty of  $+0.019$ .

At higher redshifts of  $z > 0.4$ , we expect the trend of decreasing  $dz_{\text{med}}$  and smaller uncertainty to continue due to the thickening of the Ly  $\alpha$  forest. To estimate the significance of this effect at  $z > 0.4$ , we adopt the redshift evolution estimate of  $\frac{dN}{dz} \propto (1+z)^{1.24}$  from Danforth et al. (2016) and compute expected CDFs assuming Poisson statistics as described in Section 3.3.3. This results in an expected decrease of  $\approx 0.002$  in  $dz_{\text{med}}$  between  $z = 0.4$  and  $z = 0.8$ . Similarly, the expected confidence intervals are  $\approx 25$  per cent tighter at  $z = 0.8$  relative to  $z = 0.4$ . This further motivates the expansion of our technique to higher redshifts ( $0.5 \lesssim z \lesssim 1$ ) through new COS NUV spectra of AGNs, QSOs, and blazars, especially because the current NUV archival sample is not large enough to produce an empirical CDF at  $z > 0.45$ .

### 3.5 Comparison to previous methods

An updated redshift constraint for IES 1553+113 of  $z = 0.411-0.435$  was obtained by Johnson et al. (2019) using the method ours is based on [i.e. applying the observed AGN/QSO distribution of  $\Delta z = z_{\text{sys}} - \max(z_{\text{Ly}\alpha})$  to blazars], which was used to infer the blazar’s membership with a galaxy group they identified at  $z = 0.433$ . To measure the observed distribution of  $\Delta z = z_{\text{sys}} - \max(z_{\text{Ly}\alpha})$ , they used the AGN sample from Danforth et al. (2016)<sup>3</sup>, whereas we utilize the entirety of the COS archive available through HSLA to construct an AGN sample of high-S/N Ly  $\alpha$  forest sightlines that is  $\approx 3\times$  larger. Consequently, our observed CDF of  $\Delta z = z_{\text{sys}} - \max(z_{\text{Ly}\alpha})$  is better populated at the wings, and so the resulting 95 per cent confidence interval (i.e. our redshift constraint) is more robust. Furthermore, we have shown that the precision of our redshift constraint is not significantly affected if we assume blazars to have a lower incidence of associated Ly  $\alpha$  than most AGN [see Fig. 3 and equations (1) and (3)].

Preceding this, one of the first instances of the Ly  $\alpha$  forest being used to constrain the redshift of a blazar was by Danforth et al. (2010), who utilized the Ly  $\alpha$  and Ly  $\beta$  forests in the FUV spectrum of IES 1553+113 to infer a redshift constraint of  $0.433 < z_{\text{sys}} \lesssim 0.58$  (at a  $1\sigma$  confidence limit). The redshift lower limit was set by the highest-redshift Ly  $\alpha$  line; however, this was based on a misidentification of Ni II as H I Ly  $\alpha$  and was later corrected by Danforth et al. (2016) and Johnson et al. (2019). When using the correct line identification (see Fig. 1), the redshift constraint becomes  $0.413 < z_{\text{sys}} \lesssim 0.56$ . The redshift upper limit was obtained by applying a K–S test to differentiate between the expected and observed (non-detection) CDFs of H I absorbers ( $\langle \frac{dN}{dz} \rangle$ ) over the range  $0.4 < z < 0.75$  (also see Danforth et al. 2013). This method requires binning the observed absorbers by redshift (with a chosen bin size of  $\Delta z = 0.025$ ). Moreover, the K–S test is not particularly sensitive to differences near the ends (i.e. wings) of the CDFs (see e.g. section 3.1 of Feigelson & Babu 2012). By contrast, our technique does not require binning and uses a full, empirical CDF resulting in a factor of  $\approx 5\times$  improvement in redshift constraining power.

## 4 APPLICATION OF REDSHIFT CONSTRAINT TECHNIQUE TO OTHER BLAZARS

As discussed in Section 1, blazars are useful cosmological tools primarily because of their brightness in the UV, X-ray, and  $\gamma$ -



**Table 2.** Blazars with archival *HST* UV data to which we apply our redshift constraint technique.

Name <sup>a</sup>	$z_{\text{Lit}}^b$	$\max(z_{\text{Ly}\alpha})^c$	$z_{95}^d$	Note <sup>e</sup>	<i>HST</i> proposal ID(s)
Mrk 421	0.0293	0.025 23	[0.021, 0.048]	Consistent	11520, 12025
PKS 2155–304	0.1161	0.110 29	[0.106, 0.133]	Consistent	12038
1ES 1215+303	0.131	0.116 52	[0.112, 0.139]	Consistent	13651
3C 273	0.1576	0.146 48	[0.142, 0.169]	Consistent	12038
H 2356–309	0.1654	0.165 88	[0.161, 0.188]	Consistent	12864
1ES 1118+424	0.230	0.205 72	[0.201, 0.228]	Improves	14772
S5 0716+714	0.26	0.231 46	[0.227, 0.254]	Improves	12025
3C 66A	0.340	0.334 72	[0.330, 0.357]	Consistent	12612, 12863
1ES 1553+113	0.433	0.413 06	[0.408, 0.436]	Consistent	11520, 12025, 15835
PKS 1424+240	0.6047	0.603 36	[0.599, 0.626]	Consistent	12612, 13288

Notes.<sup>a</sup>Object ID, from HSLA (see Section 4)

<sup>b</sup>Redshift estimate for blazar from the literature (see references in Section 4).

<sup>c</sup>Highest redshift Ly  $\alpha$  line detected in UV spectrum of blazar (see Section 4). For 1ES 1118+424, additional UV observations are necessary to confirm its  $\max(z_{\text{Ly}\alpha})$  (see Section 4.2).

<sup>d</sup>Redshift constraint (95 per cent confidence interval) for blazar based on the observed edge of the Ly  $\alpha$  forest obtained using our technique (see Sections 3.1, 3.3, and 4)

<sup>e</sup>‘Consistent’ indicates  $z_{95}$  is consistent with the blazar’s systemic redshift (see Section 4.1), and ‘improves’ indicates  $z_{95}$  improves the blazar’s redshift estimate (see Section 4.2).

ray. However, many blazars – so-called BL Lac objects such as 1ES 1553+113 – are so bright, relative to their host galaxy and any nuclear line emission, that intrinsic spectral features are nearly or completely undetectable, making it difficult to determine their redshifts. Despite deep observations across the electromagnetic spectrum, many such quasi-featureless blazars have no direct spectroscopic redshift measurement, and so indirect methods are required to constrain their redshifts instead, such as by associating the blazar with a nearby galaxy group (e.g. Farina et al. 2016; Rovero et al. 2016; Torres-Zafra et al. 2018; Johnson et al. 2019).

Given the agreement between our redshift constraint for 1ES 1553+113 and its inferred galaxy group association (see Sections 3.1 and 3.2), we further test the utility of our redshift constraint technique by applying it to a number of other well-known blazars that have difficult-to-measure redshifts. We searched the literature to construct a sample of nine (9) additional bright blazars that have archival *HST* UV spectra, most of which are key targets for future studies of the WHIM (Bregman et al. 2015) and for constraints on the EBL (Biteau & Williams 2015). We use our updated Ly  $\alpha$  forest based redshift estimation technique<sup>5</sup> to establish more certainty in (Section 4.1) and even improve (Section 4.2) the redshift estimates of these blazars (see Table 2). In Fig. 2, we show the positions of the blazars in relation to the adopted redshift constraint, and, in Fig. 3, we show the blazars in relation to the alternative redshift constraint that corresponds to blazars having a lower incidence of associated H I Ly  $\alpha$  (see Section 3.3.2).

<sup>5</sup>The following applications of our redshift constraint technique to blazars use equation (1) (i.e. the 95 per cent confidence interval obtained in Section 3.1). This application inherently assumes that blazars and AGNs have a similar incidence of associated Ly  $\alpha$  because the majority of the  $\max(z_{\text{Ly}\alpha})$  used to obtain our redshift constraint (i.e. equation 1) is ‘associated’ (see Section 3.3). However, this assumption may not be valid given possible differences between blazars and AGN/QSOs. Because of this, in Section 3.3.2 we explored the appropriate redshift constraint resulting from our technique if blazars and AGN/QSOs were to have different observed incidences of associated H I Ly  $\alpha$ , finding that the inferred redshift lower and upper limits would be expected to increase by only  $\approx 0.004$  and  $\approx 0.015$ , respectively (see Fig. 3 and equations 1 and 3).

#### 4.1 Constraint is consistent with blazar’s archival redshift

(i) **Mrk 421** As one of the nearest blazars to the MW, Mrk 421 is well studied for its extreme brightness and variability (e.g. Ulrich, Maraschi & Urry 1997; Abdo et al. 2011). Despite multiple X-ray observations, there are so far no confident detections of the hot WHIM towards Mrk 421 in O VII or O VIII absorption (Nicastro et al. 2005b; Kaastra et al. 2006; Rasmussen et al. 2007; Danforth et al. 2011; Yao et al. 2012; Nicastro 2014).

The redshift of Mrk 421 has been measured from intrinsic optical features, first to be  $z = 0.0300 \pm 0.0001$  (de Vaucouleurs et al. 1991) and later updated to be  $z = 0.0293 \pm 0.0001$  (van den Bosch et al. 2015). We utilize the archival COS G130M+G160M FUV spectra of Mrk 421 to identify its highest redshift Ly  $\alpha$  absorption line. Based on its  $\max(z_{\text{Ly}\alpha})$  at  $z = 0.025 23$ , we infer a redshift constraint for Mrk 421 using our technique (i.e. equation 11) of  $z_{\text{sys}} = 0.021\text{--}0.048$ , which is consistent with its systemic redshift ( $\approx 73$ rd percentile, see Fig. 2).

(ii) **PKS 2155–304** This BL Lac-type blazar is one of the highest priority sightlines for future X-ray absorption studies of the hot WHIM, given its considerable X-ray flux and comparatively long redshift path-length (Bregman et al. 2015). Tentative detections of intervening O VIII have been reported towards PKS 2155–304 (Fang et al. 2002; Fang, Canizares & Yao 2007) but have not been confirmed by follow-up observations (Rasmussen, Kahn & Paerels 2003; Yao et al. 2010; Nevalainen et al. 2019), marking the importance of future X-ray missions to clarify the possible hot gas along this sightline.

The redshift of PKS 2155–304 has been indirectly constrained through association with a nearby galaxy overdensity at  $z = 0.116$  (Falomo et al. 1991; Falomo, Pesce & Treves 1993), later confirmed and refined to be located at  $z = 0.116 10 \pm 0.000 06$  (Farina et al. 2016). We utilize the archival COS G130M FUV spectrum of PKS 2155–304 to identify its highest redshift Ly  $\alpha$  absorption line, which we confirm with the line identifications of Danforth et al. (2016)<sup>3</sup>. Based on its  $\max(z_{\text{Ly}\alpha})$  at  $z = 0.11029$ , our inferred redshift constraint for PKS 2155–304 is  $z_{\text{sys}} = 0.106\text{--}0.133$ , which is consistent with membership in the galaxy group at  $z = 0.116$  ( $\approx 79$ th percentile, see Fig. 2).

(iii) **1ES 1215+303** This TeV-detected,  $\gamma$ -ray blazar is of particular interest to the high-energy astrophysics community (e.g. Aleksić et al. 2012; Valverde et al. 2020) and is considered a priority

sightline for future X-ray studies of the WHIM (Bregman et al. 2015).

Its redshift has been determined through detection of intrinsic optical features ([O II] and [O III]) at  $z \approx 0.131$  (Paiano et al. 2017), validating the previous estimate of  $z = 0.130$  reported by Bade et al. (1998). This redshift measurement was further verified by detection of the blazar’s broad Ly  $\alpha$  emission line in the FUV (Furniss et al. 2019). We utilize the archival COS G130M+G160M FUV spectra of IES 1215+303 to identify its highest-redshift Ly  $\alpha$  absorption line. Based on its  $\max(z_{\text{Ly}\alpha})$  at  $z = 0.11652$ , our inferred redshift constraint for IES 1215+303 is  $z_{\text{sys}} = 0.112\text{--}0.139$ , which is consistent with its previously measured systemic redshift of  $z = 0.131$  ( $\approx 91$ st percentile, see Fig. 2).

(iv) **3C 273** Observations of this bright FSRQ blazar (e.g. Healey et al. 2007) have yielded some of the first reported detections of the highly ionized IGM: The FUV spectrum of 3C 273 contains intervening O VI absorption at  $z = 0.120$  (Sembach et al. 2001; Danforth & Shull 2008), and a recent X-ray follow-up study of 3C 273 reported the tentative detection of the hot WHIM through O VIII and Ne IX absorption at  $z = 0.090$  (Ahoranta et al. 2020).

The redshift of 3C 273 is known from intrinsic optical features (Mg II, [O III], and Balmer lines) found at  $z = 0.158$  (Schmidt 1963), later refined to be  $z = 0.1576$  using the [O III] line (Shang et al. 2011). We utilize the archival COS G130M FUV spectrum of 3C 273 to identify its highest-redshift Ly  $\alpha$  absorption line, which we confirm with the line identifications of Danforth et al. (2016).<sup>3</sup> Based on its  $\max(z_{\text{Ly}\alpha})$  at  $z = 0.14648$ , our inferred redshift constraint for 3C 273 is  $z_{\text{sys}} = 0.142\text{--}0.169$ , which is consistent with its systemic redshift ( $\approx 84$ th percentile, see Fig. 2).

(v) **H 2356–309** This BL Lac object is considered a top-20 AGN sightline for absorption studies of the hot WHIM (Bregman et al. 2015). So far, no detections of intervening O VII or O VIII lines have been reported towards H 2356–309, although a transient O VIII absorption feature was found intrinsic to the blazar (Fang et al. 2011). The redshift of H 2356–309 was first measured from stellar absorption features at  $z = 0.165$  (Falomo 1991) and was later refined to be  $z = 0.16539 \pm 0.00018$  by cross-correlating the host galaxy spectrum with predefined template spectra (Jones et al. 2009). Its redshift was further confirmed by the detection of its weak Ly  $\alpha$  emission line (Fang et al. 2014). We utilize the archival COS G130M FUV spectrum of H 2356–309 to identify its highest redshift Ly  $\alpha$  absorption line, which we confirm with the line identifications of Danforth et al. (2016).<sup>3</sup> Based on its  $\max(z_{\text{Ly}\alpha})$  at  $z = 0.16588$ , our inferred redshift constraint for H 2356–309 is  $z_{\text{sys}} = 0.161\text{--}0.188$ , which is consistent with its systemic redshift ( $\approx 23$ rd percentile, see Fig. 2).

(vi) **3C 66A** This BL Lac object is one of the brightest extragalactic  $\gamma$ -ray sources (e.g. Acciari et al. 2009) and has a nearly featureless spectrum, which has resulted in spurious redshift measurements over time (see Bramel et al. 2005, and references therein). The lack of a firm spectroscopic redshift measurement for this blazar motivated follow-up observations that revealed its likely association with a galaxy group at  $z = 0.340$  (Torres-Zafra et al. 2018). We utilize the archival COS G130M+G160M FUV spectra of 3C 66A to identify its highest redshift Ly  $\alpha$  absorption line, which we confirm with the line identifications of Danforth et al. (2016).<sup>3</sup> Based on its  $\max(z_{\text{Ly}\alpha})$  at  $z = 0.33472$ , our inferred redshift constraint for 3C 66A is  $z_{\text{sys}} = 0.330\text{--}0.357$ , which is consistent with its galaxy group association ( $\approx 77$ th percentile, see Fig. 2) and notably improves its previous redshift upper limit inferred using its Ly  $\alpha$  forest (Furniss et al. 2013a). We note that the updated redshift for 3C 66A of  $z = 0.34$  (Torres-Zafra et al. 2018) can be used to improve studies

of the EBL performed towards this blazar (see Domínguez et al. 2011).

(vii) **PKS 1424+240** This TeV-detected BL Lac object is one of the highest redshift known blazars and so may be useful for absorption studies of the hot WHIM and for constraints on the EBL. Its redshift has been indirectly constrained to be  $z = 0.6010 \pm 0.003$  through association with a nearby galaxy group (Rovero et al. 2016), which is consistent with its previous redshift lower limit based on its Ly  $\beta$  forest (Furniss et al. 2013b) and was subsequently refined by the identification of intrinsic emission lines ([O II] and [O III]) at  $z = 0.6047$  (Paiano et al. 2017).

We utilize the archival COS G130M+G160M FUV spectra and Space Telescope Imaging Spectrograph (STIS) NUV spectrum (PI: Furniss, PID: 13288) of PKS 1424+240 to identify its highest-redshift Ly  $\alpha$  absorption line, which we confirm with the line identifications of Danforth et al. (2016).<sup>3</sup> Based on its  $\max(z_{\text{Ly}\alpha})$  at  $z = 0.60336$ , our inferred redshift constraint for PKS 1424+240 is  $z_{\text{sys}} = 0.599\text{--}0.626$ , which is consistent with both its galaxy group association and also the detected intrinsic spectral features ( $\approx 7$ th and  $\approx 59$ th percentiles, respectively, see Fig. 2). Our redshift constraint for PKS 1424+240 significantly improves its previously inferred redshift upper limits of  $z < 0.64$  and  $z < 0.75$  based on the blazar’s  $\gamma$ -ray (Biteau & Williams 2015) and FUV (Furniss et al. 2013b) spectra, respectively. We note that this redshift constraint would be an estimated  $\approx 15$  per cent tighter if we accounted for the expected change in the evolution of H I systems (Danforth et al. 2016) over  $0.45 < z < 0.6$  (see Section 3.4).

#### 4.2 Constraint improves blazar’s redshift estimate

(i) **1ES 1118+424** There is some discrepancy surrounding the redshift of this BL Lac object (which is also known as RBS 0970 or FBQS J112048.0+421212); stellar absorption features (Ca II, Ca I, and Mg I) were detected at  $z = 0.230$  (Archambault et al. 2016), but, subsequently, a redshift lower limit of  $z > 0.28$  was inferred based on the apparent non-detection of stellar absorption features expected from the host galaxy (see Paiano et al. 2017 and references therein). We utilize the archival COS G130M FUV spectrum of IES 1118+424 to identify its highest-redshift Ly  $\alpha$  absorption line. Based on its  $\max(z_{\text{Ly}\alpha})$  at  $z = 0.20572$ , our inferred redshift constraint for IES 1118+424 is  $z_{\text{sys}} = 0.201\text{--}0.228$ , which is possibly in tension with the previous estimate of  $z = 0.230$  ( $\approx 99$ th percentile, see Fig. 2). Given the lack of G160M coverage towards this blazar, additional UV observations are necessary to confirm that there are no further H I Ly  $\alpha$  lines beyond  $z = 0.20572$ . Additional galaxy redshift surveys in the field would also be useful to further explore association with a host group.

(ii) **S5 0716+714** This bright and highly variable (Bach et al. 2007) BL Lac object is considered a top-50 AGN sightline for absorption studies of the hot WHIM (Bregman et al. 2015); however, it has no direct spectroscopic redshift measurement despite numerous attempts to detect its host galaxy (Biermann et al. 1981; Stickel, Fried & Kuehr 1993; Scarpa et al. 2000; Rector & Stocke 2001; Pursimo et al. 2002; Bychkova et al. 2006; Finke et al. 2008; Shaw et al. 2013; Paiano et al. 2017). The edge of the Ly  $\alpha$  forest towards this blazar has been used to set a statistical constraint on its redshift of  $0.2315 < z < 0.322$  (95 per cent confidence interval, Danforth et al. 2013, see description of method in Section 3.5), which was noted to be consistent with its previous redshift estimate of  $z = 0.31 \pm 0.08$  based on the tentative photometric detection of its host galaxy (Nilsson et al. 2008). Alternatively, S5 0716+714 may be associated with a nearby pair of galaxies at  $z = 0.26$  (Stickel

et al. 1993; Danforth et al. 2013). Studies of the EBL-corrected  $\gamma$ -ray spectrum of S5 0716+714 have shown both redshift estimates to be possible (Anderhub et al. 2009; MAGIC Collaboration 2018), demonstrating the need for a more confident redshift constraint for this blazar.

We utilize the archival COS G130M+G160M FUV spectra of S5 0716+714 to identify its highest redshift Ly $\alpha$  absorption line, which we confirm with the line identifications of Danforth et al. (2016).<sup>3</sup> Based on its  $\max(z_{\text{Ly}\alpha})$  at  $z = 0.23146$ , our inferred redshift constraint for S5 0716+714 using equation (1) is  $z_{\text{sys}} = 0.227\text{--}0.254$ , which provides a strong redshift constraint for this blazar. Our improved upper limit for the redshift of S5 0716+714 suggests that it may indeed be a member of the galaxy group at  $z = 0.26$  ( $\approx 99$ th percentile, see Fig. 2), especially if we assume blazars to have a lower average incidence of associated Ly $\alpha$  (see Section 3.3, Fig. 3). However, our redshift constraint for S5 0716+714 does leave open the possibility that it is located at even lower redshift, and so further deep galaxy surveys towards this blazar are necessary to confirm its redshift.

In summary, out of the ten (10) blazars we have considered in this work (Table 2), our redshift constraint technique improves the redshift estimates of two (2) blazars (IES 1118+424 and S5 0716+714, see Section 4.2) and is consistent with the systemic redshifts of the other eight (8) blazars (see Sections 3.2, 4.1). These blazars, among others, are key targets both for future X-ray missions that aim to study the WHIM (e.g. Bregman et al. 2015) and also for constraints on the EBL in the  $\gamma$ -ray (e.g. Biteau & Williams 2015). Indeed, the most X-ray bright blazars are BL Lac objects, whereas FSRQ-type blazars have systematically lower X-ray flux (e.g. Massaro et al. 2015; Mao & Urry 2017; Sharma & O’Sullivan 2021), further establishing the importance of accurate redshift constraints for featureless blazars/BL Lac objects. We have thus demonstrated the utility of the edge of the observed H I Ly $\alpha$  forest as an independent redshift constraint for blazars, which may be crucial for interpreting future studies of the hot WHIM, as we have indeed shown to be the case for IES 1553+113 (see Section 3.2).

## 5 CONCLUSIONS

In this paper, we have utilized the edge of the observed H I Ly $\alpha$  forest as a robust statistical tool to improve the precision of indirect redshift constraints for featureless blazars. We developed a technique to constrain the redshift of an AGN or blazar – with a  $1\sigma$  uncertainty of  $\approx 0.01$  – using only the position of its UV-detected, highest redshift H I Ly $\alpha$  absorption line. Our technique is based on a large sample of 192 AGNs/QSOs at  $0.01 \lesssim z \lesssim 0.45$  with high-quality COS FUV spectra, which we used to characterize the intrinsic scatter in the gap between low-redshift AGNs and the edge of the Ly $\alpha$  forest detected towards them.

We constructed the observed cumulative distribution of the difference between AGN/QSO systemic redshifts and their highest redshift Ly $\alpha$  absorption line with  $\log N_{\text{H I}}/\text{cm}^{-2} > 12.6$ ,  $\Delta z = z_{\text{sys}} - \max(z_{\text{Ly}\alpha})$ , and we use the 95 percent confidence interval of this distribution as a robust redshift constraint (see equation 1) when combined with an object’s UV-detected  $\max(z_{\text{Ly}\alpha})$ . We explored the systematics of our blazar redshift constraint technique and determined that the systematic uncertainty coming from any differences in the frequency of associated absorption and/or the proximity effect between blazars and typical AGN is sub-dominant compared to the statistical uncertainty on  $\Delta z$ .

We extended the UV spectral coverage of IES 1553+113 with new COS NUV data to confirm its highest redshift Ly $\alpha$  absorption line at  $z = 0.413$ , and we applied our Ly $\alpha$ -forest-based redshift estimation technique to this blazar. Our redshift constraint for IES 1553+113 of  $z = 0.408\text{--}0.436$  improves confidence in its inferred redshift upper limit and confirms its membership of a galaxy group at  $z = 0.433$ .

We applied our redshift constraint technique to nine other bright blazars that have archival *HST* UV spectra, most of which are BL Lac objects and key targets for studies of both the hot WHIM and the EBL. Our inferred redshift constraints for these blazars improve the redshift estimates of two (IES 1118+424 and S5 0716+714) and are consistent with previous redshift estimates for the rest. We have shown that our technique – based purely on the edge of the observed Ly $\alpha$  forest – is able to significantly improve redshift constraints for featureless blazars.

Indeed, the most X-ray bright blazars are BL Lac objects (e.g. Sharma & O’Sullivan 2021), of which a significant portion have unconstrained redshifts as a result of their featureless spectra (Bregman et al. 2015), demonstrating the importance of accurate redshift constraints for featureless blazars to interpret future studies of the hot WHIM. Another potential application of our technique that we did not explore in this work is constraining the redshifts of gamma-ray bursts (GRBs) hosted by faint galaxies, which may also be useful probes of the WHIM (Walsh et al. 2020).

Our results emphasize the need to obtain further UV and X-ray spectroscopy of blazars and AGN – complemented with deep galaxy surveys – in order to improve our understanding of the WHIM and its role in galaxy evolution. *Given the state of current UV facilities, the most immediate need is complementary UV spectra of X-ray bright AGNs and blazars in order to fully exploit future possible detections of the hot WHIM in X-ray absorption towards these sightlines.*

## ACKNOWLEDGEMENTS

We thank the reviewer for their constructive feedback that helped improve robustness of the results. This research was funded by a National Aeronautics and Space Administration (NASA) grant through *HST*-GO-15835. Support for programme #15835 was provided by NASA through a grant from STScI, which is operated by the Associations of Universities for Research in Astronomy, Incorporated, under NASA contract NAS 5-26555. This study is based on observations made with the NASA/European Space Agency (ESA) *HST*, obtained from the data archive at STScI. This work is part of the research programme Athena with project number 184.034.002 and Vici grant 639.043.409, which are financed by the Dutch Research Council (NWO). This research made use of ASTROPY, a community-developed core PYTHON package for astronomy (Astropy Collaboration 2013), as well as NUMPY (Harris et al. 2020), SCIPY (Virtanen et al. 2020), MATPLOTLIB (Hunter 2007), EMCEE (Foreman-Mackey et al. 2013), LIFELINES (Davidson-Pilon et al. 2021), and PYQT5/PYQTGRAPH. This research has made use of the HSLA data base, developed and maintained at STScI, Baltimore, USA. This research has made use of the NASA/IPAC Extragalactic Database (NED), which is operated by the Jet Propulsion Laboratory, California Institute of Technology, under contract with NASA.

## DATA AVAILABILITY

The NUV data for IES 1553+113 presented in this paper are publicly available on the Mikulski Archive for Space Telescopes (MAST, <https://archive.stsci.edu/hst/search.php>). The FUV data for

IES 1553+113 and for the AGN/QSOs and blazars used in this paper can be accessed from MAST as well as the *HST* Spectroscopic Legacy Archive (<https://archive.stsci.edu/missions-and-data/hsla>), which is available in the public domain.

## REFERENCES

- Abdo A. A. et al., 2011, *ApJ*, 736, 131
- Acciari V. A. et al., 2009, *ApJ*, 693, L104
- Ahoranta J. et al., 2020, *A&A*, 634, A106
- Ahoranta J., Finoguenov A., Bonamente M., Tilton E., Wijers N., Muzahid S., Schaye J., 2021, preprint ([arXiv:2109.12146](https://arxiv.org/abs/2109.12146))
- Aleksić J. et al., 2012, *A&A*, 544, A142
- Allen D. A., Longmore A. J., Hawarden T. G., Cannon R. D., Allen C. J., 1978, *MNRAS*, 184, 303
- Allevato V., Finoguenov A., Cappelluti N., 2014, *ApJ*, 797, 96
- Anderhub H. et al., 2009, *ApJ*, 704, L129
- Anderson M. E., Bregman J. N., 2010, *ApJ*, 714, 320
- Anglés-Alcázar D., Faucher-Giguère C.-A., Kereš D., Hopkins P. F., Quataert E., Murray N., 2017, *MNRAS*, 470, 4698
- Archambault S. et al., 2016, *AJ*, 151, 142
- Astropy Collaboration, 2013, *A&A*, 558, A33
- Bach U. et al., 2007, *A&A*, 464, 175
- Bade N., Beckmann V., Douglas N. G., Barthel P. D., Engels D., Cordis L., Nass P., Voges W., 1998, *A&A*, 334, 459
- Bajtlik S., Duncan R. C., Ostriker J. P., 1988, *ApJ*, 327, 570
- Bannister K. W. et al., 2019, *Science*, 365, 565
- Barret D. et al., 2016, in den Herder J.-W. A., Takahashi T., Bautz M., eds, Proc. SPIE Conf. Ser. Vol. 9905, Space Telescopes and Instrumentation 2016: Ultraviolet to Gamma Ray. SPIE, Bellingham, p. 99052F
- Bechtold J., 1994, *ApJS*, 91, 1
- Bergeron J., Bokserberg A., Dennefeld M., Tarengi M., 1983, *MNRAS*, 202, 125
- Bianchi L., 2014, *Ap&SS*, 354, 103
- Biermann P. et al., 1981, *ApJ*, 247, L53
- Biteau J., Williams D. A., 2015, *ApJ*, 812, 60
- Blades J. C., Hunstead R. W., Murdoch H. S., Pettini M., 1985, *ApJ*, 288, 580
- Bonamente M., Nevalainen J., Tilton E., Liivamägi J., Tempel E., Heinämäki P., Fang T., 2016, *MNRAS*, 457, 4236
- Bramel D. A. et al., 2005, *ApJ*, 629, 108
- Bregman J. et al., 2019, *BAAS*, 51, 450
- Bregman J. N., 2007, *ARA&A*, 45, 221
- Bregman J. N., Lloyd-Davies E. J., 2007, *ApJ*, 669, 990
- Bregman J. N., Alves G. C., Miller M. J., Hodges-Kluck E., 2015, *J. Astron. Telesc. Instrum. Syst.*, 1, 045003
- Bregman J. N., Anderson M. E., Miller M. J., Hodges-Kluck E., Dai X., Li J.-T., Li Y., Qu Z., 2018, *ApJ*, 862, 3
- Bu J., Ma R.-Y., Fang T.-T., Yu X.-D., Cao X.-W., 2019, *Res. Astron. Astrophys.*, 19, 153
- Burchett J. N. et al., 2019, *ApJ*, 877, L20
- Bychkova V. S., Kardashev N. S., Boldycheva A. V., Gnedin Y. N., Maslennikov K. L., 2006, *Astron. Rep.*, 50, 802
- Calverley A. P., Becker G. D., Haehnelt M. G., Bolton J. S., 2011, *MNRAS*, 412, 2543
- Cen R., Ostriker J. P., 1999, *ApJ*, 514, 1
- Cen R., Ostriker J. P., 2006, *ApJ*, 650, 560
- Chand H., Gopal-Krishna, 2012, *ApJ*, 754, 38
- Chen C., Hamann F., Simon L., Barlow T., 2018, *MNRAS*, 481, 3865
- Corwin Harold G. J., Buta R. J., de Vaucouleurs G., 1994, *AJ*, 108, 2128
- Cui W. et al., 2019, *MNRAS*, 485, 2367
- Danforth C. W. et al., 2016, *ApJ*, 817, 111
- Danforth C. W., Shull J. M., 2008, *ApJ*, 679, 194
- Danforth C. W., Keeney B. A., Stocke J. T., Shull J. M., Yao Y., 2010, *ApJ*, 720, 976
- Danforth C. W., Stocke J. T., Keeney B. A., Penton S. V., Shull J. M., Yao Y., Green J. C., 2011, *ApJ*, 743, 18
- Danforth C. W., Nalewajko K., France K., Keeney B. A., 2013, *ApJ*, 764, 57
- Davidson-Pilon C. et al., 2021, *CamDavidsonPilon/lifelines*: 0.26.0
- de Graaff A., Cai Y.-C., Heymans C., Peacock J. A., 2019, *A&A*, 624, A48
- de Vaucouleurs G., de Vaucouleurs A., Corwin Herold G. J., Buta R. J., Paturel G., Fouque P., 1991, *Third Reference Catalogue of Bright Galaxies*. Springer, New York
- Dhiman V., Gupta A. C., Gaur H., Wiita P. J., 2021, *MNRAS*, 506, 1198
- Domínguez A. et al., 2011, *MNRAS*, 410, 2556
- Dressler A., Shectman S. A., 1988, *AJ*, 95, 284
- Eckert D. et al., 2015, *Nature*, 528, 105
- Falco E. E. et al., 1999, *PASP*, 111, 438
- Falomo R., 1991, *AJ*, 101, 821
- Falomo R., Giraud E., Maraschi L., Melnick J., Tanzi E. G., Treves A., 1991, *ApJ*, 380, L67
- Falomo R., Melnick J., Tanzi E. G., 1992, *A&A*, 255, L17
- Falomo R., Pesce J. E., Treves A., 1993, *ApJ*, 411, L63
- Falomo R., Pian E., Treves A., 2014, *A&AR*, 22, 73
- Fang T., Marshall H. L., Lee J. C., Davis D. S., Canizares C. R., 2002, *ApJ*, 572, L127
- Fang T., Canizares C. R., Yao Y., 2007, *ApJ*, 670, 992
- Fang T., Buote D. A., Humphrey P. J., Canizares C. R., Zappacosta L., Maiolino R., Tagliaferri G., Gastaldello F., 2010, *ApJ*, 714, 1715
- Fang T., Buote D. A., Humphrey P. J., Canizares C. R., 2011, *ApJ*, 731, 46
- Fang T., Danforth C. W., Buote D. A., Stocke J. T., Shull J. M., Canizares C. R., Gastaldello F., 2014, *ApJ*, 795, 57
- Fang T., Buote D., Bullock J., Ma R., 2015, *ApJS*, 217, 21
- Farina E. P., Fumagalli M., Decarli R., Fanidakis N., 2016, *MNRAS*, 455, 618
- Feigelson E. D., Babu G. J., 2012, *Modern Statistical Methods for Astronomy*. Cambridge Univ. Press, Cambridge
- Finke J. D., Shields J. C., Böttcher M., Basu S., 2008, *A&A*, 477, 513
- Foreman-Mackey D., Hogg D. W., Lang D., Goodman J., 2013, *PASP*, 125, 306
- Fouqué P., Durand N., Bottinelli L., Gougouenheim L., Paturel G., 1992, *Catalogue of optical radial velocities*, Issue 3 of Monographies de la base de données extragalactiques, Observatoire de Lyon
- Fox A. J., Bergeron J., Petitjean P., 2008, *MNRAS*, 388, 1557
- Frank S., Pieri M. M., Mathur S., Danforth C. W., Shull J. M., 2018, *MNRAS*, 476, 1356
- Fukugita M., Peebles P. J. E., 2004, *ApJ*, 616, 643
- Furniss A. et al., 2013b, *ApJ*, 768, L31
- Furniss A., Fumagalli M., Danforth C., Williams D. A., Prochaska J. X., 2013a, *ApJ*, 766, 35
- Furniss A., Worseck G., Fumagalli M., Johnson C. A., Williams D. A., Pontrelli P., Prochaska J. X., 2019, *AJ*, 157, 41
- Ganguly R. et al., 2013, *MNRAS*, 435, 1233
- Gaskin J. A. et al., 2018, in den Herder J.-W. A., Nikzad S., Nakazawa K., eds, Proc. SPIE Conf. Ser. Vol. 10699, Space Telescopes and Instrumentation 2018: Ultraviolet to Gamma Ray. SPIE, Bellingham, p. 106990N
- Ghisellini G., Tavecchio F., Foschini L., Ghirlanda G., 2011, *MNRAS*, 414, 2674
- Goldoni P. et al., 2021, *A&A*, 650, A106
- Green J. C. et al., 2012, *ApJ*, 744, 60
- Gupta A., Mathur S., Krongold Y., Nicastro F., Galeazzi M., 2012, *ApJ*, 756, L8
- Harris C. R. et al., 2020, *Nature*, 585, 357
- Healey S. E., Romani R. W., Taylor G. B., Sadler E. M., Ricci R., Murphy T., Ulvestad J. S., Winn J. N., 2007, *ApJS*, 171, 61
- Helfand D. J., White R. L., Becker R. H., 2015, *ApJ*, 801, 26
- Hellsten U., Gnedin N. Y., Miralda-Escudé J., 1998, *ApJ*, 509, 56
- Hewett P. C., Wild V., 2010, *MNRAS*, 405, 2302
- Hintzen P., 1984, *ApJS*, 55, 533
- Ho L. C., Kim M., 2009, *ApJS*, 184, 398
- Huchra J. P. et al., 2012, *ApJS*, 199, 26
- Huchra J., Latham D. W., da Costa L. N., Pellegrini P. S., Willmer C. N. A., 1993, *AJ*, 105, 1637
- Huchra J. P., Vogeley M. S., Geller M. J., 1999, *ApJS*, 121, 287
- Hunter J. D., 2007, *Comput. Sci. Eng.*, 9, 90

- Hussain T., Khaire V., Srianand R., Muzahid S., Pathak A., 2017, *MNRAS*, 466, 3133
- Isobe T., Feigelson E. D., Nelson P. I., 1986, *ApJ*, 306, 490
- Johnson S. D. et al., 2019, *ApJ*, 884, L31
- Jones D. H. et al., 2009, *MNRAS*, 399, 683
- Joshi R., Chand H., Gopal-Krishna, 2013, *MNRAS*, 435, 346
- Kaasra J. S., Werner N., Herder J. W. A. d., Paerels F. B. S., de Plaa J., Rasmussen A. P., de Vries C. P., 2006, *ApJ*, 652, 189
- Kaur A. et al., 2017, *ApJ*, 834, 41
- Kellermann K. I., Sramek R., Schmidt M., Shaffer D. B., Green R., 1989, *AJ*, 98, 1195
- Kovács O. E., Bogdán Á., Smith R. K., Kraft R. P., Forman W. R., 2019, *ApJ*, 872, 83
- Kulkarni V. P., Fall S. M., 1993, *ApJ*, 413, L63
- Lyke B. W. et al., 2020, *ApJS*, 250, 8
- Macquart J. P. et al., 2020, *Nature*, 581, 391
- Madejski G. G., Sikora M., 2016, *ARA&A*, 54, 725
- MAGIC Collaboration, 2018, *A&A*, 619, A45
- Mao P., Urry C. M., 2017, *ApJ*, 841, 113
- Martizzi D. et al., 2019, *MNRAS*, 486, 3766
- Marziani P., Sulentic J. W., Dultzin-Hacyan D., Calvani M., Moles M., 1996, *ApJS*, 104, 37
- Mas-Ribas L. et al., 2017, *ApJ*, 846, 4
- Massaro E., Maselli A., Leto C., Marchegiani P., Perri M., Giommi P., Piranomonte S., 2015, *Ap&SS*, 357, 75
- Massaro F., Capetti A., Paggi A., Baldi R. D., Tramacere A., Pillitteri I., Campana R., 2020, *ApJ*, 900, L34
- McQuinn M., 2016, *ARA&A*, 54, 313
- Medlock I., Cen R., 2021, *MNRAS*, 502, 3664
- Meiring J. D., Tripp T. M., Werk J. K., Howk J. C., Jenkins E. B., Prochaska J. X., Lehner N., Sembach K. R., 2013, *ApJ*, 767, 49
- Miller M. J., Bregman J. N., 2013, *ApJ*, 770, 118
- Mishra S., Gopal-Krishna, Chand H., Chand K., Ojha V., 2019, *MNRAS*, 489, L42
- Mitchell P. D., Schaye J., 2021, preprint ([arXiv:2103.10966](https://arxiv.org/abs/2103.10966))
- Monroe T. R., Prochaska J. X., Tejos N., Worseck G., Hennawi J. F., Schmidt T., Tumlinson J., Shen Y., 2016, *AJ*, 152, 25
- Mulchaey J. S., Mushotzky R. F., Burstein D., Davis D. S., 1996, *ApJ*, 456, L5
- Muzahid S., Srianand R., Arav N., Savage B. D., Narayanan A., 2013, *MNRAS*, 431, 2885
- Muzahid S., Johnson S., Charlton J. C., Chen H.-W., Mulchaey J. S., Narayanan A., Schaye J., Wijers N., 2019, Near-Ultraviolet Follow-up of the X-ray-detected Warm-Hot Intergalactic Medium Toward IES 1553+113, *HST Proposal*
- Narayanan A., Wakker B. P., Savage B. D., Keeney B. A., Shull J. M., Stocke J. T., Sembach K. R., 2010, *ApJ*, 721, 960
- Narayanan A., Savage B. D., Mishra P. K., Wakker B. P., Khaire V., Wadadekar Y., 2018, *MNRAS*, 475, 3529
- Nevalainen J. et al., 2019, *A&A*, 621, A88
- Nicastro F. et al., 2005a, *Nature*, 433, 495
- Nicastro F. et al., 2005b, *ApJ*, 629, 700
- Nicastro F. et al., 2018, *Nature*, 558, 406
- Nicastro F. et al., 2021, *Experimental Astronomy*, 51, 1013
- Nicastro F., 2014, in Ness J.-U., ed., *The X-ray Universe*, p. 11
- Nicastro F., 2018, preprint ([arXiv:1811.03498](https://arxiv.org/abs/1811.03498))
- Nicastro F., Senatore F., Gupta A., Mathur S., Krongold Y., Elvis M., Piro L., 2016, *MNRAS*, 458, L123
- Nilsson K., Pursimo T., Sillanpää A., Takalo L. O., Lindfors E., 2008, *A&A*, 487, L29
- Ocker S. K., Cordes J. M., Chatterjee S., 2021, *ApJ*, 911, 102
- Oppenheimer B. D., Schaye J., 2013, *MNRAS*, 434, 1043
- Ostriker J. P., Vietri M., 1985, *Nature*, 318, 446
- Pachat S., Narayanan A., Khaire V., Savage B. D., Muzahid S., Wakker B. P., 2017, *MNRAS*, 471, 792
- Paiano S., Landoni M., Falomo R., Treves A., Scarpa R., Righi C., 2017, *ApJ*, 837, 144
- Paiano S., Falomo R., Treves A., Padovani P., Giommi P., Scarpa R., 2021, *MNRAS*, 504, 3338
- Pandey A., Gupta A. C., Wiita P. J., Tiwari S. N., 2019, *ApJ*, 871, 192
- Pâris I. et al., 2017, *A&A*, 597, A79
- Pascarelle S. M., Lanzetta K. M., Chen H.-W., Webb J. K., 2001, *ApJ*, 560, 101
- Peeples M. et al., 2017, *The Hubble Spectroscopic Legacy Archive, Instrument Science Report COS 2017-4*
- Peeples M. S. et al., 2019, *ApJ*, 873, 129
- Penton S. V., Stocke J. T., Shull J. M., 2004, *ApJS*, 152, 29
- Pietsch W., Bischoff K., Boller T., Doeberiner S., Kollatschny W., Zimmermann H. U., 1998, *A&A*, 333, 48
- Pursimo T., Nilsson K., Takalo L. O., Sillanpää A., Heidt J., Pietilä H., 2002, *A&A*, 381, 810
- Qu Z., Huang R., Bregman J. N., Li J.-T., 2021, *ApJ*, 907, 14
- Rajagopal M., Kaur A., Ajello M., Rau A., Domínguez A., Cenko B., Greiner J., Hartmann D. H., 2020, *ApJ*, 898, 18
- Rasmussen A., Kahn S. M., Paerels F., 2003, in Rosenberg J. L., Putman M. E., eds, *X-ray IGM in the Local Group*. Kluwer Academic Publishers, Dordrecht, p. 109
- Rasmussen A. P., Kahn S. M., Paerels F., Herder J. W. d., Kaastra J., de Vries C., 2007, *ApJ*, 656, 129
- Rau A. et al., 2012, *A&A*, 538, A26
- Rauch M., 1998, *ARA&A*, 36, 267
- Ravi V. et al., 2019, *Nature*, 572, 352
- Readhead A. C. S. et al., 2021, *ApJ*, 907, 61
- Rector T. A., Stocke J. T., 2001, *AJ*, 122, 565
- Remillard R. A., Bradt H. V., Buckley D. A. H., Roberts W., Schwartz D. A., Tuohy I. R., Wood K., 1986, *ApJ*, 301, 742
- Ren B., Fang T., Buote D. A., 2014, *ApJ*, 782, L6
- Retana-Montenegro E., Röttgering H. J. A., 2017, *A&A*, 600, A97
- Rovero A. C., Muriel H., Donzelli C., Pichel A., 2016, *A&A*, 589, A92
- Savage B. D., Kim T. S., Wakker B. P., Keeney B., Shull J. M., Stocke J. T., Green J. C., 2014, *ApJS*, 212, 8
- Scarpa R., Urry C. M., Falomo R., Pesce J. E., Treves A., 2000, *ApJ*, 532, 740
- Schmidt M., 1963, *Nature*, 197, 1040
- Schmidt M., Green R. F., 1983, *ApJ*, 269, 352
- Schneider D. P. et al., 2007, *AJ*, 134, 102
- Sembach K. R., Howk J. C., Savage B. D., Shull J. M., Oegerle W. R., 2001, *ApJ*, 561, 573
- Shang Z. et al., 2011, *ApJS*, 196, 2
- Sharma A., O'Sullivan E., 2021, preprint ([arXiv:2107.08159](https://arxiv.org/abs/2107.08159))
- Shaw M. S. et al., 2013, *ApJ*, 764, 135
- Shen Y. et al., 2011, *ApJS*, 194, 45
- Shull J. M., Danforth C. W., 2018, *ApJ*, 852, L11
- Shull J. M., Smith B. D., Danforth C. W., 2012, *ApJ*, 759, 23
- Simionescu A. et al., 2011, *Science*, 331, 1576
- Singari B., Ghosh T., Khatri R., 2020, *J. Cosmol. Astropart. Phys.*, 2020, 028
- Smith R. K. et al., 2019, in *UV, X-Ray, and Gamma-Ray Space Instrumentation for Astronomy XXI*, Vol. 111180, p. 13
- Snyder E. M., Sonnentrucker P., 2017, *Analysis of the COS/NUV Extraction Box Heights*, Instrument Science Report COS 2017-3
- Somerville R. S., Davé R., 2015, *ARA&A*, 53, 51
- Springob C. M., Haynes M. P., Giovanelli R., Kent B. R., 2005, *ApJS*, 160, 149
- Stecker F. W., Baring M. G., Summerlin E. J., 2007, *ApJ*, 667, L29
- Stickel M., Fried J. W., Kuehr H., 1988, *A&A*, 198, L13
- Stickel M., Fried J. W., Kuehr H., 1993, *A&AS*, 98, 393
- Stocke J. T., Danforth C. W., Perlman E. S., 2011, *ApJ*, 732, 113
- Tanimura H. et al., 2019, *MNRAS*, 483, 223
- Thom C., Chen H.-W., 2008, *ApJS*, 179, 37
- Tilton E. M., Danforth C. W., Shull J. M., Ross T. L., 2012, *ApJ*, 759, 112
- Torres-Zafra J., Cellone S. A., Buzzoni A., Andruchow I., Portilla J. G., 2018, *MNRAS*, 474, 3162

- Tripp T. M., Sembach K. R., Bowen D. V., Savage B. D., Jenkins E. B., Lehner N., Richter P., 2008, *ApJS*, 177, 39
- Tumlinson J., Peebles M. S., Werk J. K., 2017, *ARA&A*, 55, 389
- Tuominen T. et al., 2021, *A&A*, 646, A156
- Ulrich M.-H., Maraschi L., Urry C. M., 1997, *ARA&A*, 35, 445
- Urban O., Werner N., Simionescu A., Allen S. W., Böhringer H., 2011, *MNRAS*, 414, 2101
- Urry C. M., Scarpa R., O’Dowd M., Falomo R., Pesce J. E., Treves A., 2000, *ApJ*, 532, 816
- Valverde J. et al., 2020, *ApJ*, 891, 170
- van den Bosch R. C. E., Gebhardt K., Gültekin K., Yıldırım A., Walsh J. L., 2015, *ApJS*, 218, 10
- Véron-Cetty M. P., Véron P., 2010, *A&A*, 518, A10
- Virtanen P. et al., 2020, *Nat. Methods*, 17, 261
- Walker C. R. H., Ma Y.-Z., Breton R. P., 2020, *A&A*, 638, A37
- Walsh S., McBreen S., Martín-Carrillo A., Dauser T., Wijers N., Wilms J., Schaye J., Barret D., 2020, *A&A*, 642, A24
- Wijers N. A., Schaye J., Oppenheimer B. D., Crain R. A., Nicastro F., 2019, *MNRAS*, 488, 2947
- Wijers N. A., Schaye J., Oppenheimer B. D., 2020, *MNRAS*, 498, 574
- Wisotzki L., Christlieb N., Bade N., Beckmann V., Köhler T., Vanelle C., Reimers D., 2000, *A&A*, 358, 77
- Yao Y., Wang Q. D., Penton S. V., Tripp T. M., Shull J. M., Stocke J. T., 2010, *ApJ*, 716, 1514
- Yao Y., Shull J. M., Wang Q. D., Cash W., 2012, *ApJ*, 746, 166

## SUPPORTING INFORMATION

Supplementary data are available at *MNRAS* online.

**Table S1.** Low-redshift AGN/QSOs with high-quality HST/COS FUV data used for the redshift constraint technique.

Please note: Oxford University Press is not responsible for the content or functionality of any supporting materials supplied by the authors. Any queries (other than missing material) should be directed to the corresponding author for the article.

This paper has been typeset from a  $\text{\TeX}/\text{\LaTeX}$  file prepared by the author.